THE DEUTERON-DEUTERON REACTION AND THE STOPPING CROSS SECTION OF D_2O ICE BELOW 600 KEV

Thesis by

William A. Wenzel

In Partial Fulfillment of the Requirements
for the Degree of
Doctor of Philosophy

California Institute of Technology
Pasadena, California
1952

ACKNOWLEDGMENTS

The author would like to thank Professor T. Lauritsen, who directed the project from its inception, for valuable aid, especially in the early stages of development. Professors W. A. Fowler, R. F. Christy, and C. C. Lauritsen are to be thanked for valuable discussions on experimental and theoretical problems connected with the research. Dr. A. P. French of Pembroke College, Cambridge, kindly offered advice based on his experience with the D-D problem.

The author is especially indebted to Dr. Ward Whaling, in collaboration with whom the entire research program on cross sections was undertaken. Much of the material presented in this thesis will appear in two papers, "The Stopping Cross Section of D_2O Ice" and "Cross Section and Angular Distribution of the $D(dp)H^3$ Reaction" by W. A. Wenzel and Ward Whaling (to be published).

Thanks are due to many others whose help has been indispensable. V. F. Ehrgott has solved many of the design problems connected with the research. L. Gililland, G. Fastle, J. Hill and J. Macallister performed most of the machine shop work. W.D. Gibbs and J. Wilson assisted with the electronics. R. Peterson helped with much of the numerical work. W. Davis and Dr. E. Inonu contributed to the ion source development.

The author wishes to thank Mary Oiye, who typed this thesis and other material connected with the project.

The assistance of an Eastman Kodak Fellowship during the past year is gratefully acknowledged. The experimental work was assisted by the joint program of the Office of Naval Research and the Atomic Energy Commission.

ABSTRACT

The energy loss of protons and deuterons in D_2O ice has been measured over the energy range, $E_p = 18 - 541$ kev. The double focusing magnetic spectrometer was used to measure the energy of the particles after they had traversed a known thickness of the ice target. One method of measurement is used to determine relative values of the stopping cross section as a function of energy; another method measures absolute values. The results are in very good agreement with the values calculated from Bethe's semi-empirical formula. Possible sources of error are considered and the accuracy of the measurements is estimated to be ± 4%.

The $D(dp)H^3$ cross section has been measured by two methods. For $E_D = 200 - 500$ kev the spectrometer was used to obtain the momentum spectrum of the protons and tritons. From the yield and stopping cross section the reaction cross section at 90° has been obtained.

For $E_D = 35 - 550$ kev the proton yield from a thick target was differentiated to obtain the cross section. Both thin and thick target methods were used to measure the yield at each of ten angles. The angular distribution is expressed in terms of a Legendre polynomial expansion. The various sources of experimental error are considered in detail, and the probable error of the cross section measurements is estimated to be ± 5%.

TABLE OF CONTENTS

TABLE OF CONTENTS

LIST OF FIGURES

I. INTRODUCTION

The study of nuclear reactions involving positively charged bombarding particles of low energy is hindered by the reduction in yield brought about by the coulomb potential barrier. Therefore in work involving the light nuclei, a large current of bombarding particles is desirable for bombarding energies below half a million volts. While the electrostatic generator is an ideal source of monoenergetic particles, it can be operated stably over a voltage range of a factor of only five or ten. Moreover the inflexibility of the focusing properties of the generator usually results in a decrease in the available beam at the lower energies.

The 600 kev electrostatic generator of the Kellogg Radiation Laboratory was designed to operate in the low energy region, and emphasis was placed on obtaining a relatively large beam. Since the generator has not been described previously, a section of Part II will be devoted to a brief discussion of it, and an account of the ion source development will be given.

Because of the fundamental nature of the nuclei involved, the D-D reaction has long been of interest and has been studied extensively since the discovery by Lawrence, Lewis, and Livingston(1) in 1933 that two deuterons can react with the emission of long range protons (2),(3)...(27). The results presented in work published before 1948 are summarized by A. P. French(28).

The primary object of the work to be described was the determination of the absolute cross section and angular distribution of the reaction

$$H^2 + H^2 \longrightarrow H^1 + H^3 + 4.032 \text{ Mev}^{(29)} \qquad \text{(I-1)}$$

from 35 to 550 kev. The companion reaction

$$H^2 + H^2 \longrightarrow n + He^3 + 3.267\ \text{Mev}^{(29)} \qquad (I-2)$$

also was studied, although there is large uncertainty in the quantitative results.

In one experiment the charged reaction products from a heavy ice target were detected with a heavy particle spectrometer set at a laboratory angle of 90.3° with respect to the beam. Since the D-D reaction is very anisotropic, even at low energies, determination of the total cross section requires a knowledge of the angular distribution. This was measured in a separate experiment using a chamber in which the high energy protons were detected with a proportional counter. Measurement of total yields by this method provided another determination of the total cross section.

Since the value of the stopping cross section of deuterons in heavy ice is the largest source of uncertainty in a determination of the reaction cross section by the present method, an independent experiment to determine this factor was performed. The stopping cross section was determined from the measured yield of protons scattered into the spectrometer from the oxygen in the ice target.

The spectrometer and other apparatus used in the experiment are described in Part II. Since a cross section experiment requires the accurate knowledge of a large number of parameters, the calibration procedures are described in some detail. In Part III the experiment to determine the stopping cross section of protons in heavy ice is described, and the results are discussed. The D-D cross section and angular distribution measurements are described in Part IV, and sources of error are considered. In Part V deviations of the $O^{16}(pp)O^{16}$ scattering cross section from the Rutherford formula are calculated, and an effort is made to reconcile the present experimental values for the D(dp)H^3 cross section and angular distribution with a simple model of the interaction which has previously been applied to other experimental results(30),(31).

II. APPARATUS

1. Electrostatic Generator

The 600 kev electrostatic generator (Fig. 1) is mounted vertically in a cylindrical steel tank of length 9' and diameter 5'. The wall thickness is 27/64", and the rated working pressure is 150 psi. A flanged fitting 20 inches from the bottom permits removal of the upper section by two winches. This makes the machine easily accessible for servicing. In operation the tank is filled with air dried over KOH. A pressure of 85 psi suffices for operating voltages up to 600 kev.

The high voltage dome and ion source equipment are supported on two identical columns. Each consists of 10 porcelain insulators 2-1/2 inches high and 10 inches in outside diameter (Lapp Insulator Company, Inc., LeRoy, New York) separated by 1/8" stainless steel plates, which support the spun steel electrodes making up the column lens system. The porcelain to metal seal is made by vinylseal. Accurate alignment during sealing was achieved by the use of a specially constructed mandrel, surrounded by a furnace, which was heated to 150°C during sealing. At this time the column was put under a large compressional force by means of a torque wrench. Compression was maintained during cooling. The columns are supported on 6" steel tubes welded to the bottom of the tank. These are set 26" apart on a diameter of the tank.

To maintain a uniform potential gradient from the high voltage dome to ground, a set of ten corona rings surrounds the columns. Between the columns is a corresponding set of belt guards. Both sets are made from 3/4" tubular brass. The corona rings are about 39" in diameter. A resistor column to give equal electrical spacing between corona rings may be switched to give resistances per section of 150, 300, or 450 megohms. A cylindrical high voltage electrode is used with another set of corona rings to maintain a uniform gradient in the upper section of the tank. Twenty-three rings made of 1/2" aluminum tubing are supported on four 2" lucite posts. The rings are separated by 800 megohm resistors. The current drawn by this column is led out through a spring contact in the top of the tank and used as a rough indication of the generator voltage. This construction proved economical and has the advantage that addition of a belt above the dome should be possible if larger beam currents from the generator are required.

Control of the resistor column switching and of all the power supplies in the dome is achieved by means of eight 1" lucite rods, which lead from the bottom of the tank into the dome. The rods pass through holes in plates connected electrically to the respective corona rings. At the bottom of the tank the lucite rods connect to 3/16" steel rods which lead through pressure fittings in the tank into the control room below.

The high voltage electrode is made of sheet aluminum,rolled and "welded" to form a cylinder. The ends are slightly rounded, and corona rings similar to those described above are fitted to reduce the gradient near the ends. The length of the dome is 38" and the diameter,42". It is supported by lugs which fit four sections of channel iron fastened to a half inch steel plate on top of the columns. Also on this plate are the roller mounting and the spray combs for removing charge from the belt. A three inch brass tube leads from the beam tube to the other column. This permits differential pumping of the gas from the ion source.

A second plate, located 15" above the first, is insulated from it by lucite supports. This plate supports ion source and beam focusing supplies, including a 1500 watt permanent magnet 115 v,60 cps,generator, driven by a V-belt from the upper roller. The focusing system (Fig. 2) uses a probe, operated at 0 - 15 kev to extract ions from the source, and a focus electrode variable up to 30 kev. Normally the probe and focus electrode each draw about 300 µa.

Ion source supplies include a 5 volt, 100 ampere filament transformer, a 400 volt, 200 ma D.C. anode supply, and a 3 ampere, 120 volt D.C. magnet supply. Normal operating powers are:

Filament	40 watts
Anode	15 watts
Magnet	25 watts

In addition, the palladium leak heaters (one for deuterium and one for hydrogen) in the gas supply require about 30 watts.

The beam is extracted from the arc through a .028" hole in the bottom plate. A 3/16" hole in the probe about 3 inches from the arc limits the angular divergence of the beam and permits differential pumping of the gas. Further baffling in the focus electrode is accomplished by 1/4" holes. With this arrangement the spray current required to maintain the generator voltage at full beam was reduced by a factor of nearly two below that required when baffling and differential pumping were not used.

The spray voltage, variable up to about 40 kev, is fed by a cable into the tank to a spray comb facing the belt slightly above the line of tangency to the lower roller. Normal spray current is about 400 µa, but the generator has been operated with currents as high as 1 ma.

The cotton belt is 31" wide. It is driven by the lower steel roller and runs over the upper one, which is mounted on lucite so that it can be used in a doubler arrangement employing two spray combs in the dome and a second one near the lower roller to remove negative charge from the downward moving side of the belt. Although doubler currents as high as 200 µa have been obtained, the doubler is not used because generator stability is greater without it.

Power is supplied to the lower roller through a universal joint from a 5 H.P. 220,volt 3 phase,3500 rpm motor in a pressure housing bolted directly onto the side of the tank. The roller itself is mounted on a yoke which permits continuous adjustment of the tension in the belt. Spring loaded shock absorbers on both ends of the roller mount prevent excessive vibration. Belt tension is adjustable from outside the tank by studs connected rigidly to the shock absorbers. The belt speed is about 76 feet per second.

The main pumping system consists of two 8" diffusion pumps which were built in the Institute shops following a design of the Westinghouse Electric Company. One of these pumps is connected to each column through a 6" brass tube including a two way O-ring valve, where an ion gauge is mounted. The operating pressure read on these gauges is $3 \cdot 10^{-6}$ mm of mercury on the differential pumping side and less than $1.5 \cdot 10^{-6}$ mm on the beam tube side. With the hydrogen off, the pressure is about 10^{-6} mm on each side. The two diffusion pumps are backed by a single Cenco Hypervac forepump. A pirani type pressure gauge turns off power to the diffusion pumps and closes a solenoid operated valve between forepump and diffusion pumps in case of a large rise in pressure. A "bucket" switch protects the diffusion pumps against water failure.

The precise energy of the beam is measured by means of a 90° electrostatic analyzer preceded by a magnetic deflection of a few degrees to eliminate undesired mass components. The analyzer has a plate separation of 5/8" and a radius of curvature of about 30". About 12 kev per plate is required to deflect the 600 kev beam. The high voltage is led into the analyzer through spark plugs. Measurement is made with a Leeds and Northrup Type K potentiometer and a precision resistor stack, which is kept in a thermostated box. The analyzer and generator are regulated in a manner similar to that described by Fowler, Lauritsen, and Lauritsen(32). It has been found that the current drawn from the analyzer supply is from three to five times the beam current because of ionization by the beam. Consequently, the analyzer voltage supply must be well filtered to prevent an energy spread in the beam. The measured analyzer ripple is 0.005% at no load and 0.033% with an analyzer current of 200 μa, and an analyzer voltage of 8 kev per plate.

The absolute voltage scale was obtained by calibration against known resonances: $F^{19}(p\alpha,\gamma)O^{16}$ at 340.4 kev(33) and $Li^7(p\gamma)Be^8$ at 440 kev. Linearity of the energy scale was checked by observation of the scattered monatomic, diatomic, and triatomic beams at 172, 344, and 516 kev, respectively. In this measurement the heavy particle spectrometer field was held constant, and the analyzer voltage was varied to obtain the middle of the thick target step in each case. A carbon target was used to reduce the danger of carbon surface contamination. The calibration procedure established the energy scale to within a few tenths of a percent. No deviation from linearity was detected, although a 0.3% effect would have been observable. The energy spread of the beam is small. Evidence will be given in Part II-3 to show that it is at most a few hundred volts at 500 kev.

The generator operates stably over the voltage range from 60 to 600 kev. The maximum operating voltage could probably be increased somewhat by increasing the pressure in the tank and the voltage range of the analyzer supply.

The effect of residual pressure in the vacuum system on the operating currents of both the analyzer and the spray supply has been demonstrated. In the accelerating column the current seems to be about twice the beam current under the best operating conditions. Furthermore, the installation of a liquid air trap near, but not in, the analyzer resulted in a considerable reduction of the analyzer current for a given beam current. Presumably the installation of large cold traps would permit the use of a larger beam.

Because of the relatively large current drawn by the ion source focusing electrodes (Fig. 2), the power supplies are well filtered to reduce the ripple to less than 100 volts. Difficulties encountered in the design of an efficient ion gun are discussed by R. N. Hall(34). Aside from the ion source problem itself, problems arise in connection with space charge and magnification by the electrostatic lens system. For example, from Hall's graph on the behavior of an initially parallel beam in a field free region, it can be shown that for the 1/32" diameter beam entering the probe at 5 kev, $I_{eff} = 350\ \mu a$ if the beam is to pass through the 3/16" baffle 3 inches away. In this case $I_{eff} = I_1 + \sqrt{2}\ I_2 + \sqrt{3}\ I_3$, where I_1, I_2, and I_3 are the mass 1, mass 2, and mass 3 components, respectively, of the total current. Hence the useful current is less than 350 μa in this case.

A general relation between the angle of divergence, θ_o, of rays from a source, the angle of convergence, θ_i, of rays to the image, the magnification, m, and the potentials, ϕ_o and ϕ_i, of the object and image spaces, respectively, is

$$\theta_i = \theta_o\ (\phi_o/\phi_i)^{1/2}/m \qquad \text{(II-1)}$$

A large restriction on the useful beam may occur in the use of a precision analyzer. Let us assume that 1/8" slits restrict the beam at both ends of an electrostatic analyzer. Neglecting the small focusing in the analyzer, we find for a target 6' from the upper slit a maximum angle of convergence of 0.00178 radians. In order that the 1/32" source be focused to a 1/8" spot, we must have m = 4. For $\phi_o = 5$ kev and $\phi_1 = 100$ kev, $\theta_o = 0.03$ radians. Therefore, less than one-fourth of the total beam from the probe can be focused with these energies. In order that a large part of the beam pass through the analyzer, the magnification must be kept small. This requires that the focusing take place as far as possible from the source, that is, at the lens formed by the column and the focus electrode. For this single lens system the focus voltage is proportional to the generator voltage, and space charge limitations occur at low energies. Much more beam can be obtained above the analyzer, at low generator voltage, by an increase of the focus voltage to a high value. This weakens the second gap, of which the focal length is proportional to the ratio of the focus voltage to the gradient in the column. Focusing can now be accomplished by a variation of the strength of the first focus gap. However, the large magnification in this case prevents much of the beam from passing through the analyzer. The optimum probe and focus voltages are complicated functions of the generator voltage. The fact that a linear relation between voltages for optimum operation does not seem to hold implies that the effects described above vary in importance as the generator voltage is varied.

2. Ion Source

An attempt was made to develop a hydrogen ion source of the P.I.G. (Phillips ion gauge) type, operating continuously, for use in the electrostatic generator. In this source an arc is maintained between two cathode surfaces and a hollow cylindrical anode. An axial magnetic field of about 1000 emu confines the motion of low energy (≈ 400 ev) electrons accelerated from the cathodes, to tight spirals around the field lines, causing them to oscillate along the axis between the cathode surfaces many times before they are caught by the anode. In this way, the probability of an ionizing collision with the gas in the arc chamber is greatly increased, and the source will operate at relatively low pressures. The electron supply in the arc is maintained both by ionizing collisions and by secondary emission from positive ion bombardment of the cathode surfaces. The beam is extracted by a probe through a small hole in the center of one cathode.

The initial design, using an arc chamber of length 1-1/4 inches with a stainless steel anode and aluminum cathodes, one of which contained a 0.028" exit hole, gave a total hydrogen ion yield of about 25 μa (analyzed), containing 10 - 15% mass 1, for operating pressures between 15 and 100 microns. Mass 2 and mass 3 yields were very pressure dependent, mass 2 predominating at low pressures and mass 3 at high pressures. The characteristics were in good agreement with those obtained by Lorrain(35), except that in absolute value his pressures were lower by a factor of 5 or 10, presumably because of the larger dimensions of his arc chamber.

Operating conditions were as follows:

Arc current	20 ma
Arc voltage	400 - 500 volts
Mag. field	1000 gauss
Pressure	15 - 100 μ
Total beam	25 μa (analyzed to a 3/32" spot)
H^1 fraction	10 - 15%
Lifetime	indefinite

The source could be operated at a higher power level only with a limitation on the lifetime. For example, in operation at 100 ma arc current the lifetime was 4 hours. This limitation was due to the removal of the oxide surface layer from the aluminum cathodes. A certain amount of regeneration of the cathodes could be accomplished by the injection of air or oxygen into the source, but this procedure was on the whole unsatisfactory because of the rapid rate of deterioration.

Operating conditions were as follows:

Arc current	100 ma
Arc voltage	400 - 500 volts
Mag field	1000 gauss
Pressure	20 - 100 μ
Total beam	150 μa
H^1 fraction	10 - 15%
Lifetime	4 hours

Unless it is stated otherwise, beam measurements are made after a crude magnetic separation.

It was found that the injection of small amounts of air or oxygen increased the mass 1 ratio to as much as 40% with somewhat reduced total beam output and very little mass ∞ (air). Further increases in the ratio could be made only at the expense of the intensity of all hydrogen components, including mass 1, and an increase in that of mass ∞.

The output of this source was roughly independent of the magnetic field strength from 300 to 3000 gauss. Below 300 gauss operation ceased abruptly, and just above this point operation was slightly unsteady.

To give a better idea of what goes on inside the source, a test chamber was constructed as much as possible like the arc chamber in the ion source, except that no ions were extracted. A window was provided for observations on the core of the arc. Water cooling was provided for operation at higher power. An optical spectrometer was used to estimate the relative concentrations of H^1 and molecular hydrogen in the arc. As is well known from the color of r.f. sources, the hydrogen arc consisting largely of the mass 1 component has a deep red color due to the H_α Balmer line. The molecular spectrum covers the visible range but appears mostly blue to the eye.

When the arc current was varied from a few milliamperes to 2 amperes, no important change in the color was observed. Magnetic fields up to 5000 gauss seemed to make no difference. Sometimes for a short time the arc would appear red. Since this did not appear to be related to the operating conditions, it was assumed to be due to the liberation of a small amount of air or water vapor somewhere in the system. Unfortunately, there was no direct way of observing the yield of mass 1 which might have been extracted under the above conditions.

In an effort to improve lifetime and mass 1 ratio, different cathodes were tried. Beryllium gave about the same results as aluminum. The fact that many metals did not work as cathodes for arc voltages below 600 volts supports the argument that it is the oxide layer which is effective in the production of low voltage arcs in the case of aluminum and beryllium cathodes.

Especially low voltage operation ($V \approx 100$ v) was obtained by using for the upper cathode a pad of platinum gauze saturated with an oxide emission compound (Callite Tungsten Corporation, Type #56, Lot 101745) or a piece of barium aluminate. The arc under these conditions has a negative resistance characteristic over the usual operating range. For example, with a cathode consisting of a gauze pad saturated with emission coating, at an anode current of 2 amps the voltage of the arc was only 40 volts. With such cathodes the arc could not be maintained at currents below 100 ma without a large increase in arc voltage and a decrease in pressure. Variations on the emission coating cathodes were tried. The compound, which had initially been dissolved in acetone, was fuzed on the gauge. In other attempts it was powdered and pressed into a button. In each case the solvent was driven out as much as possible first by gentle heating. The best of these attempts improved the lifetime of the cathodes to only about 20 hours, where operation ceased, apparently due to the formation of carbon on the active surface. It was not determined whether this deposit formed because of insufficient removal of the solvent from the emission compound, or whether it came from nearby gaskets or from pump oil. Presumably more careful design of the ion source and installation of liquid air traps could improve the lifetimes.

The use of such activated cathodes in the ion source of the electrostatic generator produced mass 1 ratios of about 20% and mass 1 currents up to 30 μa. But the output was usually unsteady, probably due to the formation on the cathode of hot spots which wandered about.

Operating conditions were as follows:

Arc current	200 ma
Arc voltage	80 volts
Mag field	1000 gauss
Pressure	20 - 50 μ
Beam	150 μa
Mass 1 ratio	20%
Lifetime	20 hours

The output was found to be nearly independent of arc current above 150 ma, presumably because of the effects of space charge. In the test chamber a corresponding effect was noticed in that the core of the arc, about 3/32" in diameter for currents less than 200 ma, widened to about twice this diameter at 2 amps. In order to steady the operation of the arc, a filament cathode is now used in the generator ion source (Fig. 2). The magnetic field near the filament is relatively small and has a radial component which should help to focus the electrons into the arc chamber.

The operation of this source should more properly be compared with that of the capillary arc source, rather than that of the Finkelstein type filament source(36). As in the present source, the capillary arc source requires sufficient gas to establish an arc. The heated filament serves the function of making secondary emission easier and perhaps free from local hot spots. Since the presence of the magnetic field allows the present source to operate at pressures 5 to 10 times lower than those used in the capillary arc source, more efficient ion extraction is possible. The power put into the filament is relatively low, much lower than would be required to extract an electron current (without gas) of the order of magnitude of the arc current. In this respect the source differs from the Finkelstein source, in which the filament furnishes almost the entire anode current by thermionic emission.

The present source produces a relatively large beam, but a very low proton fraction. It will operate with the filament turned off, but the output is unsteady and the lifetime is then limited. An important function of the heated cathode seems to be that it keeps itself clean. At present the source lifetime is limited by erosion of the exit hole. This is not regarded as a serious limitation, since repair is a relatively simple operation.

Operating conditions are as follows:

Arc current	200 ma
Arc voltage	80 volts
Mag field	1000 gauss
Pressure	10 - 50 µ
Beam	150 µa
Mass 1 ratio	8%
Lifetime	150 hours

Further pursuit of a mass 1 ion source was suspended at this point because the mass 2 and mass 3 components at high intensities were required to investigate low energy reactions. The output from the source is predominantly mass 2 at low pressures and mass 3 at high pressures. Very large mass 2 yields (over 100 μa) have been obtained, but the maximum analyzed beams that have been obtained are 10, 70, and 60 μa for the mass 1, 2, and 3 components, respectively. This ion source seems to be fairly efficient, requiring about 80 watts in operation. The metal ion source inherently gives lower mass 1 ratios than glass or quartz sources because of the high recombination rate of neutral hydrogen atoms on metal surfaces. For operation at high energies the low monatomic ratio is a serious disadvantage.

A very impressive and even more efficient source was Hall's radio frequency (450 mcps) source(34), which produced a large beam with a good monatomic ratio. This source was limited in lifetime by contamination of the glass surface, and its lack of ruggedness has made it unsuited to operation in the electrostatic generator.

The low frequency (20 m cps) source of the Thoneman type(37) gives a very large ($\approx$ 95%) monatomic ratio, and the large surface area seems to eliminate the problem of wall contamination. The ion production efficiency is less than that of the high frequency source.

3. Spectrometer

The features of the double focusing magnetic spectrometer have been described by Snyder, Rubin, Fowler, and Lauritsen(38). Judd has worked out the focusing properties(39), and C. W. Li has given detailed calculations for the 16" spectrometer used in connection with the present experiment(40).

The large solid angle and nonastigmatic focus make the double focusing spectrometer well suited to yield measurements. For relating yield to cross section, however, an accurate knowledge of the spectrometer constant R_c/Ω , where R_c is the resolution due to the width of the collecting slit at the detector, and Ω is the solid angle of the instrument, is necessary. A known solid angle was determined by a reamed aperture of known diameter, at a known distance from the target. The yields of particles scattered from a copper target obtained with two such apertures of 0.125" and 0.375" diameter respectively, placed 12.7" from the target, were in excellent agreement. The fluxmeter was removed for this experiment, and the solid angles in these cases were small enough so that no difficulties from obstructions in the vacuum chamber or from distortions near the edge of the field were expected. With the circular aperture removed, the fluxmeter was inserted, and the entrance aperture was trimmed to any desired size. The value of the solid angle relative to the known value was then determined in each case from the relative counting rate of scattered particles.

Judd(38) has derived an expression for the resolution of the spectrometer. This depends essentially on geometrical considerations, but in practice is complicated by the fringing field of the magnet. Li(40) has calculated the resolution of the 16" spectrometer and obtains a value, $P/\Delta P = 231$ for a 1/4" collecting slit, where ΔP is the momentum width of the slit for particles with momentum near P. A direct measurement of the resolution was made in the course of the present work. The collector slit was replaced with two slits of width, .0223" and .0216", respectively, separated by a center to center distance of 0.1994". With the spectrometer field held constant, the generator voltage was varied to scatter protons from a thin gold layer on the target surface into first one slit and then the other. The yield as a function of generator voltage is shown in Fig. 3. The momentum resolution corresponding to a 0.1994" slit is then E/2ΔE, where E is the bombarding energy, and Δ E is the observed separation of the front edges of the two peaks. The separation is about 4 kev at 500 kev bombarding energy. Measurement of this difference to a few percent requires the elimination of effects which would result from spectrometer drift and the buildup of a contamination layer on the gold. For this reason, the generator voltage was changed back and forth to take only enough points on each peak to locate the midpoint of the leading edge. In this way, a complete set of readings could be taken several times a minute. This was repeated without interruption five or ten times. The value for the resolution of the 0.246" slit was found by this method to be 235. This is in good agreement with the value obtained by Li. The measured value was used throughout in all calculations.

This same experiment can be used to set an upper limit on the energy spread of the beam. The half-width of the front edge of one of the peaks is found to be about 420 volts. The .022 inch collector slit has a resolution of 2630, corresponding to a total energy spread of about 390 volts. The target spot used was of the order of 1/32" in diameter, and the magnification of the instrument is about 0.8. Therefore, the total energy spread due to the target spot size is about 440 volts. The half-width of the observed spectrum could be obtained from a fold of the rectangular spectrometer window, the circular target width, and perhaps a gaussian spread in energy for the beam. The accuracy of the energies given above does not warrant a calculation of this effect, but it is easily seen that the spread in beam energy cannot be more than a few hundred volts.

Spectrometer resolutions for different slits can be compared by observation of the relative yield of scattered particles. In all quantitative measurements to be discussed the resolution used was either 235 or 1650.

The scintillation counter used with the spectrometer consisted of a 5819 photomultiplier with a thin ZnS(Ag) phosphor. While this gave a very low background on account of the negligible sensitive volume, it was found to be less than 100% efficient. The efficiency was found to be 0.94 by comparison of the measured yield of scattered protons with that obtained with a thin KI(Tℓ) phosphor, which was assumed to be 100% efficient. Comparison with results using a proportional counter to observe the 3 Mev D-D protons indicates that the efficiency of the ZnS phosphor may be nearer 90 - 92% in this case. However a counting efficiency of 94% has been assumed in all results based on measurements with the ZnS phosphor.

4. Current Integrator (Fig. 4)

The total number of bombarding particles is obtained by integration of the target current. A condenser in the grid circuit of a cathode follower is charged to a predetermined voltage at which a Schmitt trigger circuit fires a thyratron, which discharges a condenser through a relay coil. When the relay is closed, the integrating condenser is discharged, and a pulse is sent to two stepping relays connected in series. These in turn operate relays to stop the counters and energize a solenoid controlled beam chopper after $n \cdot 22^m$ integrator cycles, where m = 0 or 1 and n = 1, 2, ..., 9. Special features of the integrator include an isolating cathode follower, which keeps the target potential from changing more than 17.5 volts when the integrating condenser is charged to 100 volts. A fast relay permits cycling rates up to one per second without dead-time correction. In calibration, point A is grounded, R_2 is set so that precision meter (1/2%), M, reads V_{max} volts, and the trigger circuit is adjusted to fire at this point. This adjustment has been checked frequently and has been found to vary negligibly with time. To obtain the integrator

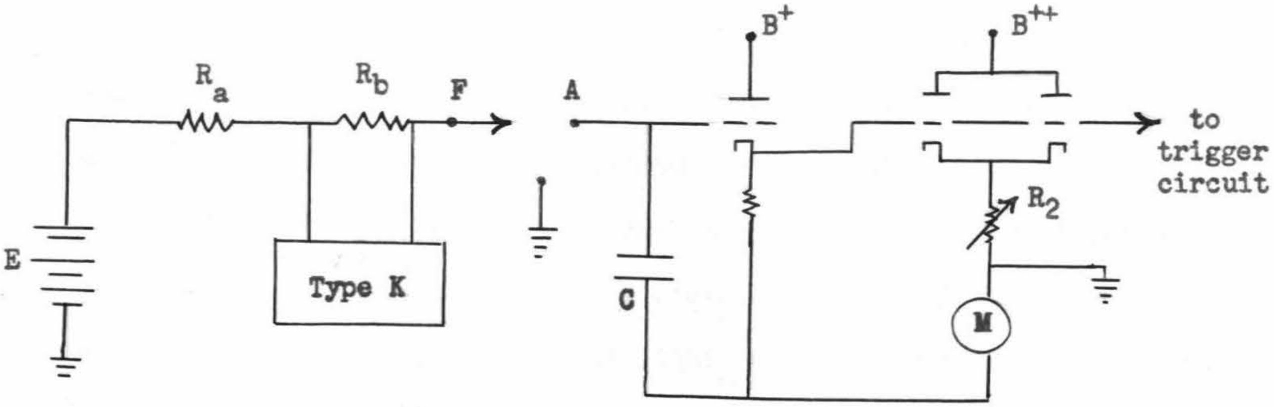

constant, battery E, precision resistors, R_a and R_b, and a Type K potentiometer were connected as shown. With point F grounded, the battery voltage is measured. With condenser C shorted, M is found to read V_{min}. If, to a good approximation, the cathode followers are linear amplifiers, it can be shown that

$$Q/T = V_{min}/(R_a + R_b) \ln(1 + V_{min}/E) \tag{II-2}$$

where Q is the charge flowing into C in an integrator cycle which lasts a time, T. We let $x = V_{min}/E$ and expand in powers of x to obtain

$$Q/T = E(1 + \frac{x}{2} - \frac{x^2}{12} + \ldots)/(R_a + R_b) \tag{II-3}$$

In the present case $V_{max} = 100$ volts, $V_{min} = 17.5$ volts, and $E \approx 300$ volts, so that the term in x^2 is negligible.

This calibration of the integrator was checked by an even more direct method, using a calibrated galvanometer with the beam itself as a source of current. Agreement was within 1%. A check after a two year interval also gave agreement within 1%. Values obtained by the first method are considered the most accurate and have been used in all calculations. In all quantitative work, charges per cycle of either 10.8 or 0.338 μ coul were used.

5. Target Chambers and Detectors

In both target chambers a cylindrical negative guard ring deflected away electrons accompanying the beam. The target itself was operated at a positive potential to prevent secondary electrons from leaving it.

In the target chamber used with the spectrometer the target was almost completely surrounded with a brass cylinder, 2.5" in diameter and 1.5" high. This was maintained at liquid nitrogen temperature in order to keep the target from being contaminated by residual vapors in the vacuum system. The vacuum measured outside this cold cylinder varied between 4 and $7 \cdot 10^{-6}$ mm of Hg. A proportional counter was mounted at $\theta_{Lab} = 150^{\circ}$ to measure the total thick target yield of the $D(dp)H^3$ reaction. Each of two counters used for this purpose had a 1/8" window covered with a 0.002" mica foil. The distances from the target were 3-15/32" and 6-11/32", respectively. The calculated solid angles should be accurate to within 2%. The yields measured with the two counters were in excellent agreement. For the angular distribution measurements a 7" diameter target chamber was constructed with windows 1/8" in diameter every 10° from $\theta_{Lab} = 10^{\circ}$ to 170° (Fig. 5). The target holder was located at the center of this chamber. A proportional counter, fixed in position opposite the window at 70°, was used as a monitor. Another counter, mounted on an arm which rotated around the center of the target chamber, could be moved in front of any window from $\theta_{Lab} = 80^{\circ}$ to $\theta_{Lab} = 170^{\circ}$. The counter windows were of mica, while those on the target chamber were of 0.001" aluminum sealed with sealstix (Central Scientific Company, Chicago, Illinois). A 4" diffusion pump and a liquid nitrogen trap between the pump and the target chamber produced an operating pressure of about 10^{-6} mm of Hg in the target chamber. The windows in the angular distribution chamber were 1/8" in diameter and 3-17/32" from the target. The relative window size at each of the ten angles, 80° to 170°, was checked with a ThC' source at the target position. The average solid angle is known to 1% and the relative solid angles with somewhat better accuracy. Since the windows in the proportional counters used were 3/16" in diameter, the windows in the chamber itself determined the solid angle. The expected loss of particles due to scattering in the windows of the target chamber is shown to be negligible by consideration of the worst case of single scattering. The probability, P, of scattering with an impact parameter less than p is given by

$$P = \pi p^2 nt \qquad \text{(II-4)}$$

where nt is the number of particles per square centimeter in the thin scattering foil. From the Rutherford formula,

$$p = \left[Z_1 Z_2 e^2 \cot(\theta/2) \right] /2E \qquad \text{(II-5)}$$

where Z_1e and Z_2e are the charges of the incident and scattering nucleus, respectively, E is the energy, and θ is the scattering angle in center of mass coordinates. In the worst case, θ is 9.1°, corresponding to a particle which grazes the aperture in the target chamber and is scattered away from the center. For 3 Mev protons passing through the 0.001" foil, this gives $P \approx 10^{-3}$. It is obvious that the effect is negligible, even for the 1 Mev protons from the $O^{16}(dp)O^{17}$ reaction.

The pulse height integral bias curve obtained with each proportional counter indicated an efficiency of 100%, within statistical uncertainties of the order of 1%.

The angular alignment of the target chamber with the beam is important. The method of measuring the spectrometer angle, θ_L, has been described(41) . For the present work $\theta_L = 90.3 \pm 0.2$ degrees. The angular distribution chamber was accurately machined in a dividing head, and holes were drilled every 10 degrees from 0° to 180°. The chamber is aligned with the beam by means of a 1/8" defining hole for the beam at $\theta_L = 180^\circ$ and a quartz window over the hole at $\theta_L = 0^\circ$.

The target holder used with both chambers is shown in Fig. 5. A copper target is soldered to the bottom of a liquid nitrogen trap. Enough insulation is provided by the re-entrant construction to permit operation for about 15 minutes without a refill of the trap.

The heavy water storage and transfer apparatus was made entirely of metals. A valve, with a differential screw for fine control of the vapor flow, could be opened to allow vapor to pass through a copper tube to a nozzle about an inch from the target surface. Instead of a packing gland, a sylphon was used to make the vacuum seal around the valve stem. The valve was closed by the contact of two solder surfaces.

III. STOPPING CROSS SECTION OF PROTONS IN D_2O (ICE)

1. Fundamental Equations and Use of the Spectrometer

The relation of measured yield to cross section must eventually come through the fundamental equation defining cross section,

$$N(E_1,\theta_c) = (d\sigma(E_1,\theta_c)/d\Omega_c)\, \Delta\Omega_c\, N_i\, n\, \Delta x \tag{III-1}$$

where $N(E_1,\theta_c)$ is the number of particles produced at energy, E_1, center of mass angle, θ_c, in solid angle, $\Delta\Omega_c$, for N_i particles incident upon a target of thickness, Δx, with n disintegrable nuclei per cubic centimeter. $d\sigma/d\Omega$ is then the differential cross section per unit solid angle at angle, θ_c, and energy, E_1.

If a thick target is used, the measured yield is an integral over thin targets, and E for charged particles decreases as the beam penetrates the target. The yield may then be expressed as

$$N(E_1,\theta_c) = \Delta\Omega_c\, N_i n \int_{E_o}^{E_1} \frac{d\sigma(E_1,\theta_c)/d\Omega}{|(dE/dx)|}\, dE \tag{III-2}$$

where E_o is the minimum energy reached by the bombarding particles in the target. Differentiating (III-2), we obtain

$$\frac{dN}{dE_1} = \frac{d\sigma}{d\Omega_c} N_i\, \Delta\Omega_c \Big/ \left|\frac{1}{n}\frac{dE_1}{dx}\right| \tag{III-3}$$

where the value of the integrand at the lower limit has been neglected, since we will deal with charged bombarding particles. We now define

$$\left|\frac{1}{n}\frac{dE_1}{dx}\right| \equiv \epsilon_1 = \text{stopping cross section} \tag{III-4}$$

where ϵ_1 depends on the target material and the energy and nature of the bombarding particle.

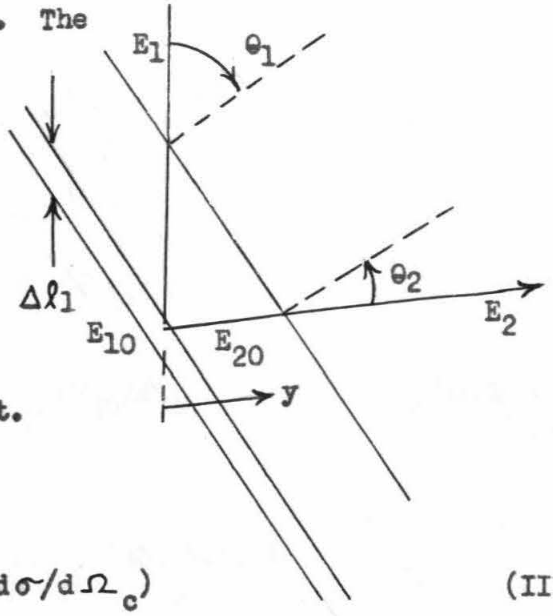

The use of the spectrometer introduces additional complications, because the energy of the reaction product detected is determined by the magnetic field of the spectrometer. The measured yield is from a layer of the target in which the bombarding particle, slowed to energy E_{10}, produces a particle at energy E_{20}, which is slowed to energy E_2 before leaving the target. The observed yield is given by

$$N(E_1,E_2,\theta_c) = \Delta\Omega_c\, N_i n\, \Delta \ell_1\, (d\sigma/d\Omega_c) \qquad \text{(III-5)}$$

where $\Delta \ell_1$ is determined by the conditions on ΔE_2; that is,

$$E_2/2\,\Delta E_2 = R_c \qquad \text{(III-6)}$$

(III-5) may now be written

$$N(E_1,E_2,\theta_c) = \frac{d\sigma}{d\Omega_c}\, \Delta\Omega_c\, E_2\, N_i/2R_c \left|\frac{1}{n}\frac{dE_2}{d\ell_1}\right| \qquad \text{(III-7)}$$

$$\left|\frac{1}{n}\ \frac{dE_2}{d\ell_1}\right| = \epsilon_{eff} \qquad \text{(III-8)}$$

From the figure above we may determine ϵ_{eff}.

$$E_2 = E_{20} + \int_0^{\ell_1 \frac{\cos\theta_1}{\cos\theta_2}} \frac{dE_2}{dy}\, dy \qquad \text{(III-9)}$$

$$\frac{dE_2}{d\ell_1} = \frac{dE_{20}}{d\ell_1} + \frac{\cos\theta_1}{\cos\theta_2}\left[\frac{dE_2}{dy}\right]_{E_2} + \int_0^{\ell_1 \frac{\cos\theta_1}{\cos\theta_2}} \frac{d}{d\ell_1}\left(\frac{dE_2}{dy}\right) dy \qquad \text{(III-10)}$$

$$= \frac{dE_{20}}{dE_{10}}\,\frac{dE_{10}}{d\ell_1} + \frac{\cos\theta_1}{\cos\theta_2}\left[\frac{dE_2}{dy}\right]_{E_2} + \left[\frac{dE_2}{d\ell_1}\right]_{y=0}^{y=\ell_1 \frac{\cos\theta_1}{\cos\theta_2}} \qquad \text{(III-11)}$$

Using the relation that $dE_2/dE_{20} = \epsilon_2/\epsilon_{2o}$, we may write

$$\epsilon_{eff} = \left|\frac{1}{n}\frac{dE_2}{d\ell_1}\right| = (\epsilon_2/\epsilon_{20}) \left[\epsilon_{10}\,(dE_{20}/dE_{10}) + \epsilon_{20}\,(\cos\theta_1/\cos\theta_2)\right] \qquad \text{(III-12)}$$

For observations on the surface of the target, $\epsilon_2 = \epsilon_{20}$, and (III-7) reduces to the form given by Snyder, et al.$^{(38)}$.

$$N_{max} = 4\pi(d\sigma/d\Omega_c)\,\Omega_c\,E_2 q/R_c\,\epsilon_{eff}\,. \qquad \text{(III-13)}$$

where q is in microcoulombs if each bombarding particle carries a single charge, $d\sigma/d\Omega_c$ is in millibarns per steradian, E_2 is in electron volts, and ϵ_{eff} is in units of 10^{-15} ev cm^2.

2. Absolute Yield Method.

To determine ϵ_{D_2O} over the proton energy range, 200 - 540 kev, protons were scattered from the O^{16} in the ice target. The stopping cross section is related to the scattering cross section by (III-13). Theoretical evidence will be presented in Part V to show that deviations of $d\sigma/d\Omega$ from the value given by the Rutherford formula are negligible. As an experimental check on this, protons were scattered from a quartz target for several bombarding energies. The target arrangement is shown in Fig. 6. The observed spectra are shown in Fig. 7. At each energy, the spectrum of protons scattered from the oxygen is superimposed on the spectrum of protons scattered from the silicon. The fluxmeter current (or voltage) is inversely proportional to the momentum of the particles being analyzed. In this case the stopping cross section is the same for protons scattered from both Si^{28} and O^{16}, aside from a small correction for the fact that E_2 is slightly less for O^{16} because of the larger recoil energy of the nucleus.

The Rutherford cross section is

$$d\sigma_c/d\Omega_c = r_o^2 \; Z_1^2 Z_2^2 \; (m_o c^2/E_c)^2 \; / \; 16 \sin^4(\theta_c/2) \qquad \text{(III-14)}$$

where $r_o = 2.82 \cdot 10^{-13}$ cm, Z_1 and Z_2 are the charge numbers of incident and target nucleus, respectively, m_o is the mass of the electron, c = $3 \cdot 10^{10}$ cm/sec., E_c is the energy, $d\sigma_c/d\Omega_c$ is the scattering cross section per unit solid angle, and θ_c is the angle of scattering, all in center of mass coordinates. With correction for center of mass motion, (III-14) may be written in laboratory coordinates as follows:

$$d\sigma_L/d\Omega_L = r_o^2 \; Z_1^2 Z_2^2 \; (m_o c^2/E_1)^2 \left[1 + \alpha^2(1+3\cos\theta)(1-\cos\theta)\right] / \; 16 \sin^4(\theta/2) \qquad \text{(III-15)}$$

to order α^2, where α is the ratio of the mass of the incident particle to that of the target particle. From (III-13) and (III-15) we predict, after making a few minor corrections, that $2N_{Si}/N_o = (14/8)^2 = 3.06$, where N_{Si} and N_o are the number of counts obtained due to silicon and oxygen scattering, respectively. Observed ratios are shown in Table III-1.

TABLE III-1

Scattering of Protons from SiO_2 (quartz)

E_1	$2N_{Si}/N_o$
361 kev	3.12
413	2.90
465	3.04
516	3.07
542	3.29
Average	3.08
Theoretical	3.06

The deviations of the experimental ratios from the predicted ratio are within experimental uncertainties. Hence, any large deviation of O^{16} scattering from the Rutherford law would imply that Si^{28} deviates in the same way.

A typical spectrum of protons scattered from the oxygen in D_2O, obtained with a solid angle of 0.00490 ± 0.00005 steradians, is shown in Fig. 8. N_{Max} is obtained by extrapolating the slight rise on the top of the step to the energy, E_2, at the midpoint of the step. Also shown in Fig. 8 by the open points are results obtained with an ice surface which had become contaminated with a layer of carbon. Thus, the condition of the ice layer, which was too thin to be seen, could be monitored continuously. With Ω_L, R_c, and q obtained by the methods explained in Part II-3 and II-4, ϵ_{eff} is determined from (III-13).

Since ϵ_{eff} depends on both E_1 and E_2, the assumed energy dependence of ϵ will affect the calculated value of ϵ from ϵ_{eff}. Since $E_2 = 0.88\ E_1$ in this case, a linear variation of ϵ, such that $\epsilon(E) = A+BE$, where A and B are constants, is a good approximation. In this case it follows easily that for $\cos\theta_1 = \cos\theta_2$

$$\epsilon(\bar{E}) = \epsilon_{eff}\,(1 + dE_2/dE_1)^{-1} \qquad \text{(III-16)}$$

where

$$\bar{E} = (E_2 + E_1\, dE_2/dE_1)(1 + dE_2/dE_1)^{-1} \qquad \text{(III-17)}$$

Thus at bombarding energies of 578, 516, 413, 310, and 258 kev, $\epsilon(\bar{E})$ has been determined for $\bar{E}$ = 542, 484, 387, 291, and 242 kev, respectively. These values are plotted in Fig. 9 as solid circles.

3. Relative Stopping Cross Section

The method of measuring ϵ described above was not satisfactory for protons of energy less than 200 kev. Some of the low energy protons capture an electron in the target and emerge as neutral H atoms which can not be deflected in the magnetic field. The amount of this charge neutralization is difficult to measure accurately. A further difficulty at very low energies is the reduced efficiency of the scintillation counter.

The following method for measuring relative values of ϵ depends only on the measurement of energy ratios and is independent of counter efficiency and neutralization of incident or scattered particles. The energy, E_{20}, of protons scattered from the surface of a clean Cu target is determined accurately from the midpoint of the step in the spectrum. When a thin layer of ice is then formed on the Cu surface, this step is displaced to a lower energy, and to return the step to its original position the bombarding energy must be increased by an amount, ΔE_a. If now ΔE_a is measured for two proton energies, using the same ice layer, then $\Delta E_a' / \Delta E_a = \epsilon'_{eff} / \epsilon_{eff}$, and the relative values of ϵ_{eff} are thereby determined. Deuterons can be used as the incident particle, and intercomparison between deuterons and protons can be made.

Calculation of the effective energies at which the ratio of the stopping cross section has been determined is somewhat complicated. In the accompanying figure, particles of bombarding energy, E_a, pass through the ice layer of thickness, t, reaching the surface of the copper with energy, E_1. They are scattered with energy, E_2, and emerge with energy, E_{20}. With no ice layer $E_a = E_1 = E_{ao}$. If $e \equiv \left|\frac{dE}{dx}\right|$, and ΔE_a is the change in generator voltage necessary to compensate for the energy loss in the ice, then to a good approximation

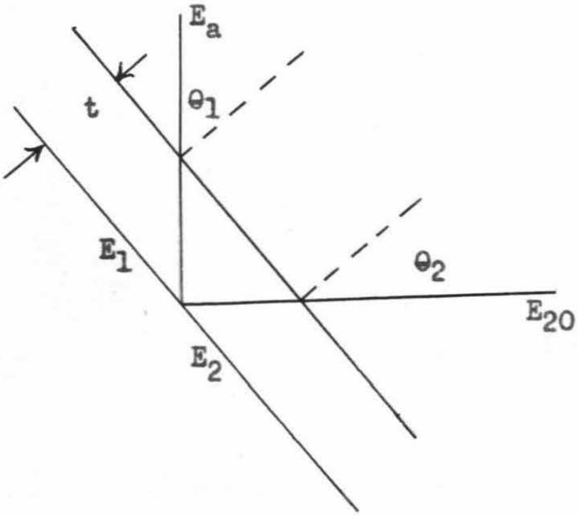

$$\Delta E_a = E_a - E_{ao} = t\left[e(\bar{E}_1)/\cos\theta_1 + e(\bar{E}_2)/\cos\theta_2(dE_2/dE_1)\right] \equiv \bar{t}\; e(\bar{E}) \tag{III-18}$$

where $\bar{E}_1 = (E_a + E_1)/2$

$$\bar{E}_2 = (E_{20} + E_2)/2 = (E_1 - \Delta E_a/2)/(dE_2/dE_1)$$

and $\bar{t}$ and $\bar{E}$ are some effective thickness and energy, respectively. If the stopping cross section is assumed to vary linearly with energy over the range of interest, such that

$$e(E) = e(\bar{E}) + m(E - \bar{E}) \tag{III-19}$$

where m is a constant, then (III-18) becomes

$$\Delta E_a = \frac{t}{\cos\theta_1}\left[1 + \left(\frac{\cos\theta_2}{\cos\theta_1}\frac{dE_2}{dE_1}\right)^{-1}\right]\left\{e(\bar{E}) + m\left[\bar{E}_1 - \bar{E} + (\bar{E}_2 - \bar{E})\left(\frac{\cos\theta_2}{\cos\theta_1}\frac{dE_2}{dE_1}\right)^{-1}\right]\right.$$

$$\left.\left[\frac{\cos\theta_2}{\cos\theta_1}\frac{dE_2}{dE_1} + 1\right]^{-1}\right\} \equiv \bar{t}\;\; e(\bar{E}), \text{ provided} \tag{III-20}$$

and

$$\bar{t} = (t/\cos\theta_1)\left[1 + (\cos\theta_2/\cos\theta_1)^{-1}(dE_2/dE_1)^{-1}\right]$$

$$\bar{\bar{E}} = \frac{\left[\bar{E}_1\left(1 + \frac{\cos\theta_2}{\cos\theta_1}\right) - \Delta E_a/2\right](dE_2/dE_1)}{1 + \frac{\cos\theta_2}{\cos\theta_1}\ \frac{dE_2}{dE_1}}$$

but

$$\bar{E}_1 = E_a - t\ e(\bar{E}_1)/2 \cos\theta \approx E_a - t\ \Delta E_a/2\bar{t} \cos\theta_1$$

therefore

$$\bar{\bar{E}} \approx \left\{ \frac{E_a\ 1 + \frac{\cos\theta_2}{\cos\theta_1} - \frac{-E_a}{2}\left[1 + \frac{\left(1 + \frac{\cos\theta_2}{\cos\theta_1}\right)\frac{\cos\theta_2}{\cos\theta_1}\ \frac{dE_2}{dE_1}}{1 + \frac{\cos\theta_2}{\cos\theta_1}\ \frac{\text{o}E_2}{\text{o}E_1}}\right]}{1 + \frac{\cos\theta_2}{\cos\theta_1}\ \frac{dE_2}{dE_1}} \right\} \frac{dE_2}{dE_1} \qquad \text{(III-21)}$$

For protons scattered from copper at $\theta = 90.3^\circ$, and $\theta_1 = 45^\circ$, this gives

$\bar{\bar{E}} = .984\ E_a - .489\ \Delta E_a$, while for deuterons (III-22)

$\bar{\bar{E}} = .969\ E_a - .477\ \Delta E_a$

Because $t/\bar{t}$ depends on the mass of the scattered particle through the factor dE_2/dE_1, comparison of ϵ's by the use of both deuterons and protons requires introduction of a factor $\bar{t}_p/\bar{t}_d$, so that

$$\epsilon_d/\epsilon_p = 0.983\ \Delta E_{ad}/\Delta E_{ap} \qquad \text{(III-23)}$$

Rapid comparison over a very wide range of proton energy was made possible by accelerating a mixture of D and H ions in the Van de Graaff generator. Using the H^+ beam component, measurements were made of ΔE_1 at the energy, E_1, of the generator. Then, simply by changing the electrostatic analyzer to pass the DD^+ and HHD^+ ions, measurements were made of ΔE_1 for the deuterons of energy, $E_1/2$, which have the same momentum as protons of energy, E_1. The measured ΔE_1 is the same as that for protons of energy, $E_1/4$, since it has been shown theoretically and confirmed experimentally that the stopping cross sections for protons and deuterons of the same velocity are equal(42). Time consuming changes of the generator voltage were thereby avoided.

This method requires that the thickness of the ice layer, usually about 3 kev, remain constant while the displacement of the step is located for two different energies. The measurements must be made as rapidly as possible, since the cold target surface will collect residual water and oil vapors present in the vacuum system. ΔE_a was measured first at one energy and then at the other, and the two measurements were repeated alternately four or five times in succession to establish their ratio. Any condensation of foreign material on the target could be detected by a change in the value of ΔE_a.

The relative measurements of ϵ_{eff} were corrected to give the value of ϵ at a particular energy in the manner described above. This function, $\epsilon(E)$, was then normalized to fit the absolute values above 200 kev. The experimental points are shown in Fig. 9 by the open circles.

4. Discussion of Errors and Uncertainties

The 4% probable error of the measurements arises from the uncertainty in the experimental quantities listed in Table III-2 .

At pressures between 10^{-6} and 10^{-7} mm Hg the neutral component of the incoming beam is negligible for protons above 200 kev. A correction for the small neutral component in the scattered beam has been made using Hall's(43) measurements of the electron capture to loss ratio in several metals. This correction to ϵ is only 3% at 240 kev, the lowest energy at which absolute measurements were made.

TABLE III-2

Sources of the Experimental Error, and Percentage Error Introduced in Final Value of ϵ_{D_2O}

Beam integrator	2%
Neutralization of incident and scattered protons	<1%
Spectrometer resolution	2%
Spectrometer solid angle	1%
Scattering cross section	<1.5%
Counter efficiency	2%
Probable error in ϵ ,	4%

The most likely source of error in the measurements of the relative values of ϵ is non-uniformity of the target thickness, such that the change from one beam component or energy to another caused a different thickness of target to be bombarded. The beam on the target was restricted to a spot approximately 1/16" in diameter, and variation in the thickness over so small an area does not seem likely. Some uncertainty is introduced in the relative measurements at very low energies by energy straggling in the target. The step in the scattered proton spectrum for the clean Cu target has a very small width, δE, determined by the resolution of the spectrometer, $E/\delta E \approx 800$, and the position of the step, taken to be the energy corresponding to half the maximum yield, N_{max}, is sharply defined. When the step is displaced by a layer of ice, straggling in the ice rounds off the step and gives it a width amounting to 25% of the displacement in the worst cases. If the straggling is truly gaussian, the energy at half maximum will still determine the displaced position of the step, but it is not so sharply defined as before. Measurements using the $N_{max}/3$ energy for the position of the step gave the same relative values for ϵ. Both the uncertainty due to straggling and possible target non-uniformities would be expected to introduce random deviations rather than a systematic error and may account for some of the spread in the experimental points at low energies.

The assumption that the target material was actually D_2O, instead of some other compound of O and D, was not checked, but the reproducibility of the experimental results at high energy indicates that the composition was constant. The assumption that dE/dx is the same for protons and deuterons of the same velocity has not been tested experimentally to better than 5%(42), but close equality seems reasonable on theoretical grounds.

Values of the stopping cross section, taken from the smooth curve drawn through the experimental points in Fig. 9, are listed in Table III-3. Previous measurements of ϵ_{H_2O} are shown by the dashed curve in Fig. 9, taken from ref. (44). The agreement is satisfactory below 100 kev, but for higher proton energy the present values lie far above the dashed curve, based in this region on Crenshaw's measurements of dE/dx in water vapor.

The dot-dashed curve in Fig. 9 shows the theoretical value for $2\epsilon_H + \epsilon_O$ computed by Hirschfelder and Magee(45) from Bethe's semi-empirical theory of stopping power; the empirical constants were evaluated from the range data for natural alpha particles. The theoretical expression will not apply near the peak of the stopping cross section curve, and the theoretical curve has not been extended below 300 kev. In the region 300 - 550 kev, the agreement between the theoretical and experimental values is within experimental error. Below 300 kev there is no satisfactory theory. The more detailed treatment of Bethe's theory by Walske(46) will probably hold at somewhat lower energies, but unfortunately it does not apply simply to light atoms such as oxygen.

One is tempted to conclude from the good agreement between the experimental values of ϵ_{D_2O} (ice) and the theoretical values of $2\epsilon_H + \epsilon_O$

TABLE III-3

The Molecular Stopping Cross Section, $\left|\frac{1}{N}\frac{dE}{dx}\right|$, for Protons in D_2O Ice

E_p(kev)	$\epsilon(10^{-15}$ ev-cm^2)
18	15.6
20	17.4
30	20.4
40	22.6
50	23.5
60	24.0
70	24.1
80	24.0
100	23.7
125	23.0
150	22.2
200	20.1
300	16.0
400	13.3
500	11.6
540	11.2

that Bragg's Law for the addition of stopping cross sections holds very well for water. However, there have been no accurate experimental checks on these theoretical values of ϵ_{H_2} and ϵ_{O_2}. In addition, there is some experimental evidence(42),(47),(48) that $\epsilon_{H_2} + \epsilon_{O_2}/2$, ϵ_{H_2O} (vapor), and ϵ_{H_2O} (liquid) differ among themselves by more than 10%. There have been no previous measurements of ϵ_{H_2O} (ice).

IV. D-D CROSS SECTION AND ANGULAR DISTRIBUTION

1. Spectrometer Observations

Fig. 10 shows a typical spectrum of the protons and tritons from the $D(dp)H^3$ reaction observed at 90.3°. Momentum separation of the protons and tritons occurs because of the motion of the center of mass relative to the laboratory coordinates. Because of the large variation with laboratory angle of the energy of particles from the D-D reaction, the spectrometer aperture was closed to reduce the solid angle to about 0.00127 steradians. This corresponds to a spread in laboratory angle of about 1°.

From (III-13) the cross section is obtained from the value of N_{Max} obtained by extrapolation of the trailing edge of the spectrum to the midpoint of the high energy edge and the values of ϵ_{D_2O}, determined by the methods described in Part III.

Cross section measurements with the spectrometer were not extended to energies below 200 kev, because the energy dependence of the cross section makes extrapolation of the trailing edge of the spectrum subject to large uncertainties.

2. 150° Thick Target Yield

The total thick target proton yield at $\theta_L = 150°$ was obtained with both target chambers. Two proportional counters used with the first (spectrometer) target chamber gave results in excellent agreement. Still another counter was used with the angular distribution chamber. The 150° yield as a function of energy is plotted in Fig. 11.

3. Angular Distribution

The angular distribution as a function of energy was obtained by both thin and thick target techniques. In the former method, feasible for bombarding energies above 200 kev, a thin layer of ice was deposited on the target, set at about 45° to the incident beam. The ratio of the counting rate at an angle, θ_L, measured by the movable counter, to the rate at 70°, measured by the monitor counter, was obtained for $\theta_L = 80^\circ$ to $\theta_L = 170^\circ$ in 10° intervals. From the observed ratios and the kinetics of the reaction the angular distribution in the center of mass system was obtained. A smooth curve was drawn through the experimental points from $\theta_c = 90^\circ$ to $\theta_c = 180^\circ$. This is sufficient to obtain the total distribution because of the necessary symmetry of the reaction in center of mass coordinates. The angular distribution was then expanded in Legendre polynomials. The effective energy at which the thin target yields were obtained was calculated in each case from the absolute thin target yield at 150° and the slope of the total thick target yield at 150°. i.e.,

$$\bar{E} = E_1 - \frac{1}{2}\frac{n(\bar{E},\ 150^\circ)}{(dN(E,\ 150^\circ)/dE)_{E_1}} \qquad \text{(IV-1)}$$

$n(E,\ 150^\circ)$ is the thin target yield,

E_1 is the bombarding energy,

$\bar{E}$ is the energy at which the angular distribution has been measured.

The thickness of the targets used varied from 20 - 50 kev over the range, 193 - 539 kev. It was found that a given target varied less than 10% in thickness while measurements were being taken at all angles. The thin target angular yield as a function of energy and angle, normalized to an arbitrary fixed target thickness, is plotted in Fig. 12.

Because of the large energy dependence of the reaction cross section at low energies, it was not feasible to use thin ice targets at energies below about 200 kev. Therefore, the total thick target yield also was obtained for each angle over the energy range, 34.3 - 516 kev. The observed yields are presented in Table IV-1. Angular distributions were obtained from this data by differentiating, with respect to energy, the total yield curve at each angle to obtain the equivalent thin target yield. Experimental angular distributions are plotted in Fig. 13. The thin target points are the solid circles, while values represented by the open circles were obtained from thick target data.

4. Total Cross Section

Knowing the cross section at some angle and the angular distribution, we may obtain the total cross section. Fig. 14 shows the results obtained in several ways. One method uses spectrometer data at 90.3° and the angular distribution obtained by thin target methods. A second method uses the excitation function at $\theta_L = 150^\circ$ and the thin target angular distribution, while a third plot is obtained from the integral over all angles of the differential cross section obtained by differentiating the thick target yield at each angle.

TABLE IV-1

Total Thick Target Yield D(dp)H^3 + O^{16}(dp)O^{17}

Counts per microcoulomb per steradian.

θ_{Lab} E(kev)	80°	90°	100°	110°	120°
516	6.83	6.58	6.64	7.10	7.62 • 10^5
465	5.56	5.28	5.40	5.60	6.05 • 10^5
413	4.11	4.01	4.01	4.26	4.53 • 10^5
362	3.28	3.17	3.14	3.33	3.56 • 10^5
310	2.37	2.29	2.33	2.46	2.61 • 10^5
258	1.708	1.580	1.615	1.688	1.828 • 10^5
206.5	1.148	1.103	1.113	1.166	1.207 • 10^5
181	.890	.871	.868	.897	.937 • 10^5
155	6.20	6.04	6.10	6.23	6.52 • 10^4
129	4.31	4.21	4.21	4.32	4.47 • 10^4
120.6	3.94	3.83	3.79	3.89	4.07 • 10^4
103.2	2.72	2.52	2.54	2.55	2.69 • 10^4
86.0	1.695	1.618	1.630	1.635	1.700 • 10^4
77.5	1.263	1.247	1.263	1.258	1.332 • 10^4
68.8	.954	.913	.910	.937	.945 • 10^4
51.5	4.01	3.73	3.71	3.85	3.84 • 10^3
34.3	.955	.949	.915	.944	.891 • 10^3

TABLE IV-1 (Cont.)
Total Thick Target Yield $D(dp)H^3 + O^{16}(dp)O^{17}$
Counts per microcoulomb per steradian

θ_{Lab} E(kev)	130°	140°	150°	160°	170°
516	8.45	9.12	10.15	11.15	$11.39 \cdot 10^5$
465	6.76	7.48	8.15	8.92	$9.08 \cdot 10^5$
413	5.01	5.55	6.04	6.52	$6.67 \cdot 10^5$
362	3.88	4.16	4.47	4.92	$4.98 \cdot 10^5$
310	2.84	3.10	3.31	3.60	$3.71 \cdot 10^5$
258	1.99	2.11	2.27	2.43	$2.54 \cdot 10^5$
206.5	1.305	1.367	1.462	1.561	$1.591 \cdot 10^5$
181	.997	1.073	1.137	1.190	$1.220 \cdot 10^5$
155	7.00	7.38	7.77	8.25	$8.36 \cdot 10^4$
129	4.82	4.98	5.21	5.59	$5.68 \cdot 10^4$
120.6	4.35	4.37	4.72	4.96	$4.91 \cdot 10^4$
103.2	2.90	2.95	3.10	3.31	$3.33 \cdot 10^4$
86.0	1.818	1.845	1.908	2.01	$2.02 \cdot 10^4$
77.5	1.380	1.415	1.472	1.572	$1.560 \cdot 10^4$
68.8	1.013	1.056	1.069	1.119	$1.103 \cdot 10^4$
51.5	4.00	4.05	4.16	4.38	$4.50 \cdot 10^3$
34.3	.945	.941	1.005	1.065	$1.083 \cdot 10^3$

$O^{16}(dp)O^{17}$ Cross Section

A difference at high energy between spectrometer results and the total yield results was attributed to the $O^{16}(dp)O^{17}$ reaction. Correction for this was made by the use of the spectrometer to measure the $O^{16}(dp)O^{17}$ cross section at 90°. Two proton groups result from reactions with Q-values of 1.95 and 1.08 Mev, respectively$^{(49)}$. With a proportional counter as a detector, to eliminate the He^3's from the D-D reaction, the spectra shown in Fig. 15 were obtained for the two groups. Under the assumption that there is no nearby resonance the cross section for each group is expected to follow very closely the asymptotic form predicted for a strong coulomb barrier, i.e.,

$$\sigma_T \propto E^{-1} \exp\left(-2\pi Z_1 Z_2 e^2/\hbar v_r\right) \tag{IV-2}$$

where σ_T is the total cross section at energy, E, Z_1e and Z_2e are the respective charges of the colliding nuclei, $\hbar = 1.055 \cdot 10^{-27}$ erg sec., and v_r is the initial relative velocity of the colliding nuclei. In this case, the effect of the barrier on the reaction products is probably not negligible, but the energy dependence would not be as large as that of the initial process.

Because of the steepness of the trailing edge of the observed spectra, it was felt that better values for the cross sections might be obtained from a fit to a Gamow plot, than from the extrapolation method used for the $D(dp)H^3$ reaction. This was done for spectra obtained at a bombarding energy of 516 kev (Fig. 16). The yield of the reaction is negligible below 400 kev. The cross sections obtained from the plots shown in Fig. 16 are:

Long Range Group

$$4\pi(d\sigma/d\Omega)_{90^\circ} = 0.5 \cdot 10^{10}\, E_{kev}^{-1} \exp\left(-355\, E_{kev}^{-1/2}\right) \text{ millibarns} \tag{IV-3}$$

Short Range Group

$$4\pi(d\sigma/d\Omega)_{90^\circ} = 1.2 \cdot 10^{10}\, E_{kev}^{-1}\, \exp(-\,355\, E_{kev}^{-1/2})\ \text{millibarns} \qquad \text{(IV-4)}$$

Correction of the $D(dp)H^3$ cross section (Fig. 14) was made on the assumption that, for the $O^{16}(dp)O^{17}$ reaction,

$$\sigma_{Total} = 4\pi\left(\frac{d\sigma}{d\Omega}\right)_{90^\circ} \qquad \text{(IV-5)}$$

The yields listed in Table IV-1 are not corrected for the $O^{16}(dp)O^{17}$ yield.

6. Errors and Uncertainties in the $D(dp)H^3$ Cross Section Measurement

(a) Apparatus Calibration

The determination of the energy scale, integrator and spectrometer constants, counter efficiencies, and solid angles are discussed in Part II.

An additional check on the spectrometer constant R_c/Ω can be obtained from a comparison of the integrated proton spectrum obtained with the spectrometer, with the thick target yield obtained at 90° with the angular distribution chamber. In this case

$$\frac{N(E,\ 90^\circ)}{q_p \Omega_p} = \frac{R_c}{q_s \Omega_s}\int_0^\infty \frac{n(I)\,dI}{I} \qquad \text{(IV-6)}$$

where $N(E,\ 90^\circ)$ is the total yield obtained by the thick target method and $N(I)$ is the observed spectrometer spectrum as a function of fluxmeter current, taken with a proportional counter detector. The subscripts, p and s, refer to the thick target yield and to the spectrometer method, respectively. The factor, $1/I$, in the integrand occurs because the spectrometer window is proportional to the momentum. The total yield obtained with the angular distribution chamber must be corrected for the $O^{16}(dp)O^{17}$ yield. The results are shown in Table IV-2.

TABLE IV-2

Proton Yield at $\theta_L = 90^\circ$

E_D(kev)	Thick Target $N/q\,\Omega$ D-D + O-D	 O-D	 D-D	Spectrometer $(R_c/q\Omega)\,(n(I)/I)dI$
206	$1.09 \cdot 10^5$	-	$1.09 \cdot 10^5$	$1.06 \cdot 10^5$
310	2.33	-	2.33	2.29
413	4.01	$.02 \cdot 10^5$	3.99	3.97
516	6.53	.12	6.41	6.38

The agreement in each case is well within experimental uncertainties.

(b) Spectrum Analysis

The procedure of extrapolating the trailing edge of the observed spectrometer spectrum to obtain N_{max} has been justified in the following way. From the experimental values for the reaction and stopping cross sections and the angular distribution, the expected spectrum for the tritons and protons was calculated (Fig. 17). The trailing edge in each case is seen to be quite straight in the vicinity of N_{max}. The experimental agreement in the case of the proton spectrum indicates that the efficiency of the scintillation counter may be less than 94%, as was suggested in Part II. The experimental triton spectrum has a long tail not shown in Fig. 17. This is presumably the result of straggling and multiple scattering, more serious effects in the case of the slower and less energetic tritons which have lost a large amount of energy in escaping from the target.

(c) Target Contamination

The heavy water used contained 99.8% deuterium. Reaction yields were reproducible over a period of three months, after the reservoir was refilled. Contamination of the target occurred with poor vacuum in the target chamber. This was attributed to the condensation of ordinary water on the target. Under good operating conditions such contamination was negligible.

Target contamination by the beam would tend to increase the relative concentration of deuterium. If we assume that the incident charge is deposited over a volume equal in cross section to the size of the beam spot, and in depth to the range of the bombarding particles, we find that for 50 kev deuterons a contamination of the order of 1% would exist after 1000 microcoulombs of bombardment. However, if the contamination tends to collect on the surface of the target, a serious error in measured yield might be expected. By a frequent renewal of the target surface this effect can be avoided. No time dependent change of yield which could be attributed to this cause was ever observed.

(d) Beam Contamination

A comparison of the reaction yields from the monatomic, diatomic, and triatomic ions indicated that the beam contamination was low. The DD^+ and the DDD^+ yields were regularly somewhat higher than the D^+ yield, but this effect never exceeded 3% and seemed to be independent of energy. Contamination of the D^+ beam by the HH^+ ions would not be expected to produce even this much effect if it resulted from the 1/2% impurity in the supply to the ion source. Presumably the somewhat larger contamination comes from the production of H_2 gas from oil vapor and gaskets. In another check on beam contamination the magnitude of the H^+ beam was found to be of the order of 1% of the D^+ beam under the same generator operating conditions.

(e) Secondary Emission

The negative guard ring in front of the target and the positive target potential reduced the danger of an electron current to or from the target. Moreover, failure to take these precautions produced at most a 5% change in yield for a bombarding energy of 34.3 kev. Similarly, a magnet brought near the incident beam to remove electrons had no observable effect on the total yield.

(f) Beam Neutralization

The beam neutralization at 51.5 kev was measured by the use of a deflecting magnet in the 60 cm length between the analyzer and the target chamber. The magnet was located about 5 cm from the target chamber. With the beam coming through the analyzer, the ratio of the $D(dp)H^3$ yield with the beam off and on the target gives directly the percentage of neutralization. With the normal operating pressure of $1.0 \cdot 10^{-6}$ mm of Hg in the target chamber and $4 \cdot 10^{-6}$ mm of Hg between the analyzer and target chamber, the neutralization measured was $\approx 0.7\%$. When air was admitted to the analyzer, raising the ion gauge pressures to $5 \cdot 10^{-6}$ mm of Hg and $2.5 \cdot 10^{-5}$ mm of Hg, respectively, the measured neutralization was about 3%. Measurement of the neutralization at lower energies was not feasible because of the relatively low yield. However, both Bartels(50) and Keene(51) have found that the electron capture cross section of protons in hydrogen increases by less than a factor of two when the bombarding energy decreases from 25 to 17.5 kev. These energies correspond to 50 and 35 kev, respectively, for bombarding deuterons.

Kanner(52) finds that the capture cross section in air is of the same order of magnitude as in hydrogen. On the basis of these results, no correction for beam neutralization has been made.

(g) Beam Intensity

A large beam power would tend to evaporate the ice by heating the target. The maximum allowable power may be estimated from the thermal properties of the target. We assume that the beam power, P, is released at the surface of a semi-infinite material of conductivity, k, with temperature, T_∞, a long way from the surface. Then if T is the temperature inside the conductor we have

$$\nabla^2 T = 0 \qquad \text{(IV-7)}$$

except at the source of power,

and

$$\int_S (\vec{\nabla} T)_n \, dS = - P/k \qquad \text{(IV-8)}$$

where S is any surface enclosing the power source. For a point source at the origin, a solution of (IV-7) and (IV-8) which gives $T = T_\infty$ at $r = \infty$, where r is the radial coordinate, and $(\vec{\nabla} T)_n = 0$ along the surface of the conductor, is:

$$T = T_\infty + P/2\pi kr \qquad \text{(IV-9)}$$

If P is spread out uniformly over a disk of radius, R, the temperature at the origin, the hottest spot, may be obtained by a simple integration and is

$$T_o = T_\infty + P/\pi kR \qquad \text{(IV-10)}$$

In the present case R = 1/16". For copper, k = 1 cal/cm sec.-degree, and the temperature rise, $T_o - T_\infty \approx (1/2)$ degree/watt. For ice, using the value for k at room temperature, we find that $T_o - T_\infty \approx 100$ degrees/watt. The actual case is somewhere in between, depending somewhat on the thickness of the ice layer, but it can be seen that the maximum beam power is restricted. The highest power used in the present work was about 2 watts. As a check against neutralization or ionization in the immediate vicinity of the target, the beam current on a 1/8" diameter target spot was varied from 0.3 to 1.8 microamperes, for a bombarding energy of 51.5 kev. There was no observable difference in yield.

(h) Statistical Errors

For the thin target angular distribution data, the statistical uncertainty of the yield at each angle is less than 4% at every energy. Total thick target yields at each angle vary from about 3% to less than 1% in statistical uncertainty from low to high energies.

(i) Differentiation Errors

At low energies the cross section is expected to have the form,

$$\sigma(E) \propto E^{-1} \exp(-44.4\, E_{kev}^{-1/2}) \qquad \text{(IV-11)}$$

and the stopping cross section

$$\left|\frac{1}{n}\frac{dE}{dx}\right| \propto E^{1/2}\ ^{(53)} \qquad \text{(IV-12)}$$

Hence the total yield $N(E_o)$ is given by

$$N(E_o) \propto \int_0^{E_o} E^{-3/2} \exp(-44.4\, E^{-1/2}) \propto \exp(-44.4\, E_o^{-1/2}) \qquad \text{(IV-13)}$$

For each angle $N(E,\theta)\exp(44.4\, E^{-1/2}) \equiv F(E,\theta)$ was plotted as a function of energy. For $E \leq 200$ kev $F(E,\theta)$ was found to be an almost linear function of energy, and differentiation was possible with some accuracy.

$$dN(E,\theta)/dE = \exp(-44.4\ E^{-1/2})\left[dF(E,\theta)/dE + 22.2\ F(E,\theta)E^{-3/2}\right] \quad \text{(IV-14)}$$

Moreover, for low energies, the term in F is much larger than the term in dF/dE. Therefore, it is felt that differentiation does not produce any large error at low energies.

In the energy range, 100 - 500 kev, it was found that the total yield varied approximately as E^2. A plot of $N(E,\theta)$ vs E^2 for each θ yielded more consistent results for dN/dE than semilog plots of $N(E,\theta)$ vs E and of $N(E,\theta)$ vs $E^{-1/2}$. At energies above 150 kev, differentiation introduces some uncertainty into the measured cross section and thick target angular distribution results. An estimate of the uncertainties may be obtained from a comparison of the angular distribution and cross section obtained by the use of both thin and thick target techniques. Values of σ_T and the angular distribution coefficients are listed in Table IV-3 for some energies. The values in each case are taken from a smooth curve drawn through the experimental points. Deviation from zero of the experimental values for the P_6 (cosθ) term in the angular distribution is considered to be an indication of the experimental uncertainties of the method. Furthermore, the amount of P_4 (cosθ) present at low energies is subject to large uncertainties. Efforts to place limits on this indicate that C_4 (Fig. 13) is of order .02 for energies below 100 kev, but this value is uncertain by almost 100%.

(j) Stopping Cross Section

Since the experiment measures the ratio of the reaction cross section to the stopping cross section, ϵ, the uncertainties in the measurements of ϵ, described in Part III, appear in σ_T (DD) as well. It is significant that certain possible systematic errors cancel out

TABLE IV-3

$D(dp)H^3$ Total Cross Section and Angular Distribution

$$d\sigma/d\Omega = (\sigma_T/4\pi)\left[1 + C_2P_2(\cos\theta) + C_4P_4(\cos\theta) + C_6P_6(\cos\theta) + \cdots\right]$$

E_{kev}	σ_T mb	C_2	C_4
35	1.94	.155	.02
50	4.81	.195	.02
70	9.49	.247	.02
100	15.8	.310	.023
150	23.8	.400	.031
200	30.6	.470	.045
250	37.0	.523	.062
300	43.1	.566	.080
350	48.1	.601	.103
400	52.3	.632	.126
450	55.8	.660	.150
500	59.0	.684	.175
550	62.0	.704	.203

when both experiments are considered together. For example, an error in the integrator constant would produce a corresponding error in the calculated value of ϵ, but not in the $D(dp)H^3$ cross section. An error in the spectrometer constant, R_c/Ω, would directly affect ϵ, but not the reaction cross section obtained with the spectrometer. In fact, the spectrometer has effectively measured the ratio of the $D(dp)H^3$ cross section to the $O^{16}(pp)O^{16}$ scattering cross section. Here we have assumed that $\epsilon_{D_2O}/\epsilon_{air}$ is the same for protons of 500 kev and 3 Mev. Values for ϵ_{air} were obtained from the literature(54). But, since ϵ_{eff} depends about half as much on ϵ_2 for the emitted protons as on ϵ_1 for the incident deuterons, the uncertainties in ϵ_{air}

should have only a small effect on the results. The stopping cross section for the tritons is obtained directly from the results of Part III.

(k) Agreement with Previous Results

The yield at low energies is about 25% lower than that obtained by Bretscher, et al.(23), using the same technique. No explanation for this can be offered. Agreement with Sanders, et al.(27) in the low energy region is very good, and the agreement with McNeill and Keyser(26) in the middle energy range is good. The techniques used by these workers are very different from those of the present work, and the agreement is encouraging. Regarding the angular distribution, the agreement with the results of Bretscher, et al., and of Sanders, et al., is good, although the finite amount of P_4 $(\cos\theta)$ which is found in the present work makes exact comparison difficult.

(l) Probable Error

Assignment of a probable error to the experimental values is difficult because of the large number of uncertain factors which enter the experiment. Most of these are involved in the value of ϵ_{D_2O} and were discussed in Part III, where a probable error of 4% was assigned to ϵ_{D_2O}. If the $D(dp)H^3$ cross section were based on the thick target yield alone, additional errors due to solid angle, counter efficiency, target and beam contamination, energy calibration, neutralization and statistics would raise the probable error to slightly over 5%. However, as was suggested before, the tendency of systematic errors to cancel from the spectrometer measurements would tend to reduce the error, except for the difficulties involved in accurate extrapolation of the spectrum. The good agreement of the spectrometer results, using both protons and tritons, with the results from the excitation function is significant.

In consideration of the above uncertainties, a probable error of 5% has been assigned to the values of the total cross section given in Table IV-3. These are taken from the solid curve of Fig. 14. It is felt that cross section values obtained from the total excitation function are more accurate than those obtained with the spectrometer, especially at energies below 300 kev.

7. $D(dn)He^3$ Reaction

Efforts were made to measure the $D(dn)He^3$ cross section by observations on the He^{3+} and He^{3++} particles, using the spectrometer. For the following reasons there is much doubt concerning the results obtained:

(a) The stopping cross section of α-particles in D_2O (ice) is not known, and there is no way of measuring it in the present experiment.

(b) The angular distribution is not known accurately.

(c) The large stopping cross section, ϵ_2, for the He^3's results in a very low yield.

(d) The He^3's have less energy than the tritons and are masked completely by the tail of the triton spectrum if a thick target is used.

(e) Scattered deuterons mask the He^{3++} yield at bombarding energies above 350 kev.

(f) $O^{16}(dp)O^{17}$ protons interfere with measurement of the He^{3+} yield at energies above 400 kev.

(g) The neutral He^3's cannot be measured.

To obtain values for the D(dn)He^3 cross section from observed yields the following assumptions were made:

(a) He^3 and He^4 particles of the same velocity have the same stopping cross sections.

(b) The stopping cross section curve for α's in D$_2$O has the same shape as the stopping cross section curve for α's in air. The latter is obtained from ref. 54.

(c) The angular distribution is the same for the D(dn)He^3 as for the D(dp)H^3 reaction.

(d) The number of neutral He^3's can be neglected.

In obtaining the yield of He^3's at each energy, a relatively thin layer of ice was used, and observations were taken above and below the step in the momentum spectrum to check the background due to low energy tritons. The background in all cases was less than 10% of N_{max}. ϵ_2 was obtained by normalizing the air curve to the D$_2$O curve at 500 kev with the value of ϵ_{D_2O} obtained from Part II^I and of ϵ_{air} for protons from ref. 54.

The values obtained for the cross section (Table IV-4) differ greatly from those obtained for the D(dp)H^3 cross section.

TABLE IV-4

E_D kev	150	200	250	300	350
σ(D(dp)H^3) mb	23.8	30.6	37.0	43.1	48.0
σ(D(dn)He^3) mb	22.6	39.6	37.5	76.7	96.5

Although the difference is well outside statistical uncertainties, the yield ratio He^{3++}/He^{3+} was observed to decrease from about 3.5 to 2.5 as E_2 increased from 0.728 to 0.779 Mev. The opposite effect is expected and has been observed to occur for α-particles in mica(55),(56),(57).

In addition, failure of the yields to repeat within statistical limits indicates that background from deuteron scattering or the $O^{16}(dp)O^{17}$ reaction may not have been negligible. This would account for the smaller difference at low energies. Results presented in ref. 26 for the energy range, 120 - 250 kev, indicate that the branching ratio is almost exactly 1 to 1.

An error in ϵ_2 in the present work would introduce a nearly constant factor into the calculated cross section. For example, if we normalize ϵ_2 by assuming that at each energy $\epsilon_{air}(p)/\epsilon_{air(\alpha)} = \epsilon_{D_2O}(p)/\epsilon_{D_2O}(\alpha)$, then the values for $\sigma\left[D(dn)He^3\right]$ given in Table IV-4 would be lowered by about 30%. It is apparent that no strong conclusions about the $D(dn)He^3$ cross section can be drawn on the basis of the present work.

V. THEORETICAL CONSIDERATIONS

1. $O^{16}(pp)O^{16}$ Cross Section

Deviations of the scattering cross section $O^{16}(pp)O^{16}$ from the Rutherford formula are to be expected for two reasons:

(a) Atomic Electron Cloud

Since the range of the potential due to the atomic electron cloud is long compared with the wave-length of the scattered proton, we can expect that a calculation of the perturbation of the classical trajectory will lead to a good estimate of the deviation of the cross section from the Rutherford law, brought about by the presence of the atomic electron cloud.

The angle between asymptotes of the classical motion of the scattered particle is given by

$$\emptyset/2 = \int_0^{u_{Max}} du \left\{ 2MP^{-2} \left[E - V(u) \right] - u^2 \right\}^{-1/2} \qquad \text{(V-1)}$$

where u = the reciprocal of the radial coordinate, M = the reduced mass of the system, E = the energy in the center of mass system, P = the angular momentum, V(u) = the potential energy of the system. $u = u_{max}$ is obtained by setting the radical in the integrand equal to zero. For the potential, V(u), one might use the Fermi-Thomas model, but calculations would be difficult. Since the shape of the perturbing potential is probably not important, the following simple form will be used:

$$V(u) = Z_1 Z_2 e^2 u - \Delta \quad \text{for } u > 1/a$$

$$V(u) = 0 \quad \text{for } u < 1/a$$

where Δ = the absolute value of the potential at the nucleus due to the electron cloud, $a = Z_1 Z_2 e^2/\Delta$, Z_1 and Z_2 are the atomic numbers of incident and target particle, respectively, and e is the electronic charge. Foldy$^{(58)}$ gives $\Delta = 34(Z_2)^{7/5}$ ev, from values based on the Hartree model of the atom. For scattered protons this gives $a = 0.794\ a_o/(Z_2)^{2/5}$, where $a_o = 0.529 \cdot 10^{-8}$ cm. This is fairly consistent with the value for an effective radius of the Fermi-Thomas atom, $a = 0.885\ a_o/(Z_2)^{1/3}$. Equation (V-1) may now be integrated directly. Introducing the impact parameter, $p = P\left[2ME\right]^{-1/2}$, the classical distance of closest approach, $b = Z_1Z_2e^2/E$, and expanding in powers of p/a and Δ /E, we obtain

$$\phi/2 = \phi_o/2 + (\ \Delta\ /4E)\ \text{ain}\ \phi_o \tag{V-2}$$

where ϕ_o is the value of ϕ in Equation (V-1) given by setting $\Delta = 0$. We note that the correction term is independent of first order terms in p/a. This tends to confirm the assumption that the shape of the potential due to the electronic cloud is not important. Hence

$$\theta - \theta_o = \delta\ \theta = -\ (\ \Delta\ /2E)\ \sin\ \theta_o \tag{V-3}$$

where $\theta = \pi - \phi$ is the scattering angle. To find the correction to the scattering cross section, we use the usual relation, $(d\ \sigma(\theta)/d\Omega)d\Omega = 2\pi p\ dp$, where $d\Omega$ is the differential solid angle, and $d\ \sigma(\theta)$ is the differential scattering cross section at the angle, θ. Since $2\pi p\ dp = 2\pi\ \sin\ \theta_o\ d\ \theta_o\ (d\ \sigma_R(\theta)/d\Omega)_{\theta_o}$, where $d\ \sigma_R$ is the Rutherford cross section, we obtain

$$\left\{\frac{d\sigma(\theta)/d\Omega - d\sigma_R(\theta)/d\Omega}{d\sigma_R(\theta)/d\Omega}\right]_{\theta_o} = -\left\{d(\delta\ \theta)/d\theta + \delta\theta \cdot \right.$$

$$\left. \cdot \left[\cot\ \theta + \frac{d(d\sigma_R(\theta)/d\Omega)/d\theta}{d\sigma_R(\theta)/d\Omega}\right]\right\}_{\theta_o} \tag{V-4}$$

Substituting Equation (V-3) in Equation (V-4) gives:

$$\left\{\frac{d\sigma(\theta)/d\Omega - d\sigma_R(\theta)/d\Omega}{d\sigma_R(\theta)/d\Omega}\right\}_{\theta_0} = -\frac{\Delta}{E} \qquad (V\text{-}5)$$

For $O^{16}(pp)O^{16}$ scattering at 200 kev this correction is only - 0.3% and has been neglected.

(b) Nuclear Interference

The scattering cross section for a spin 1/2 particle incident upon a spin 0 nucleus is given by$^{(59)}$

$$\frac{d\sigma(\theta)}{d\Omega} = \frac{1}{k^2}\left\{\Big| -\frac{n}{2}\csc^2\frac{\theta}{2}\exp\left(i n\,\ln \csc^2\frac{\theta}{2}\right)\right.$$

$$+\sum_{\ell=0}^{\infty} P_\ell(\cos\theta)\exp(i\alpha_\ell)\Big[(\ell+1)\sin\delta_\ell^+\exp(i\delta_\ell^+) + \ell\sin\delta_\ell^-\exp(i\delta_\ell^-)\Big]^2$$

$$\left. + \sin^2\theta\left|\sum_{\ell=1}^{\infty} P'_\ell(\cos\theta)\exp(i\alpha_\ell)\Big[\sin\delta_\ell^+\exp(i\delta_\ell^+) - \sin\delta_\ell^-\exp(i\delta_\ell^-)\Big]\right|^2\right\}$$

where

$$\exp(i\alpha_\ell) = (\ell + i n)/(\ell - i n)\ \ldots\ (1 + i n)/(1 - i n);\quad \ell > 0 \qquad (V\text{-}6)$$

$$\exp(i\alpha_0) = 1$$

$$P'_\ell(\cos\theta) = d\,P_\ell(\cos\theta)/d(\cos\theta)$$

where v = velocity of relative motion, M = reduced mass of the system, $\delta_\ell\,\pm$ are the phase shifts between incident and reflected wave for the ℓ'th partial wave, where the total angular momentum of the system is $J = (\ell \pm \frac{1}{2})$. Because the Coulomb barrier factor will tend to favor the lowest partial wave, and because no resonances involving higher partial waves have been discovered in the energy range to be considered, we shall restrict our attention to interference from S-wave nuclear scattering. The effect of a "hard sphere" P-wave phase shift has been estimated by R. G. Thomas(60) to be negligible.

For S-wave interference only, (V-7) becomes

$$\frac{d\sigma(\theta)}{d\Omega} = \frac{1}{k^2} \left| -\frac{\eta}{2} \csc^2 \frac{\theta}{2} \exp\left(i\eta \ln \csc^2 \frac{\theta}{2}\right) + \sin \delta_o \exp\left(i\delta_o\right) \right|^2 \qquad \text{(V-7)}$$

and

$$\cot \delta_o = -\frac{H_o \Phi_o + \left(f - \overset{*}{\Phi}_o / \Phi_o\right)^{-1}}{C_o^2 \, x \, \Phi_o^2}$$

where $H_o \Phi_o$, Φ_o, $\overset{*}{\Phi}_o / \Phi_o$ are Coulomb functions tabulated by Bloch, et al.(61),

and

$$x = ka, \quad C_o^2 = \frac{2\pi\eta}{e^{2\pi\eta} - 1}$$

$$f = \frac{ka}{u} \frac{du}{d(kr)}$$

$$a = \text{nuclear radius}$$

$u = u(r) = r\Psi_R(r)$, where $\Psi_R(r)$ is the radial part of the wave function. By fitting experimental data on the location of $S_{1/2}$ resonances in F^{17} and its mirror nucleus, O^{17}, and the value of the $O^{16}(nn)O^{16}$ scattering cross section at thermal energies, R. G. Thomas(60) has evaluated f over the energy range of interest, using a nuclear radius $a = 5.27 \times 10^{-13}$ cm. From this information, δ_o and $d\sigma/d\Omega$ have been determined for bombarding protons of energy, 400 - 600 kev. $d\sigma/d\Omega$ is plotted for several angles in Fig. 18. At a scattering angle of 90° the correction to the Rutherford formula is + 1.5% at 600 kev (f = 2.52). Since the effect depends strongly on the barrier factor in this energy region, it is quite small at lower energies and has been neglected throughout.

2. D-D Cross Section and Angular Distribution

Attempts to fit the experimental results on the D-D reaction with a relatively simple model of the nuclear interaction have been successful in accounting for the general behavior of the cross section and angular distribution with energy. Although the experimental uncertainties in the work considered by Konopinski and Teller(30) are quite large, while Beiduk, et al.(32) were able to use the experimental results on both cross section and angular distribution in the 0.6 - 3.5 Mev region, the conclusions reached were the same in both cases in at least one respect. It was impossible to fit the experimental results without the introduction of considerable spin-orbit coupling in the nuclear interaction. It was observed, for example, that without spin-orbit coupling, the introduction of enough D-wave interaction to account for the rise in the total cross section, even below 500 kev, would produce a large $\cos^4\theta$ term in the angular distribution. However, in the present work considerable $\cos^4\theta$ is found, even in the low energy region. Moreover, the fit by Beiduk, et al., at low energies was to the results of Bretscher, et al.(23) which disagree with the present results. An attempt to fit the results of different observers in different energy regions has the disadvantage that systematic errors tend to be serious. In the present work, a large energy range was covered, and the experimental uncertainties are considered to be low.

For these reasons, it seemed that an attempt to fit the present results in the bombarding energy range, 35 - 550 kev, should be made using the simpler theory considered in ref. 30. It would have been desirable that this include the results of Hunter and Richards(25), and of Blair, et al.(24), for $E_D = 0.6 - 3.5$ Mev, but this was not done because of the larger amount of work involved, the fact that the W.K.B. approximation used is not good for energies near the top of the Coulomb barrier, and the fact that the nuclear matrix elements introduced in the simplified theory may not be constant over a wide energy range.

The absence of resonances is implied by the smooth variation with energy of the angular distribution and total cross section. The increase of the asymmetry with energy implies that the higher partial waves need be considered in accordance with their ability to penetrate the Coulomb barrier.

Two deuterons can collide in singlet, triplet, and quintet spin states. Since the deuteron is a Bose particle, the total wave function must be symmetric with respect to an interchange of the particles, and the singlet and quintet can occur only with even orbital states, while the triplet occurs only with odd orbital states.

The final state, involving two spin 1/2 particles which are not identical, may be triplet or singlet with all orbitals. Following the usual procedure(30),(31), we neglect all initial quintet states and the final triplet states with zero orbital angular momentum for the reason that the exclusion principle tends to prevent the close approach of identical nucleons with parallel spins.

The Coulomb barrier will tend to suppress initial states of high ℓ . The energy release of the reaction is high enough ($\approx$ 4 Mev) to permit orbitals up to F-wave in the final state, without essential modification by the barrier. If we consider only initial states with $\ell \leq 2$, we must consider the transitions shown in the accompanying diagram. Spectroscopic notation is used.

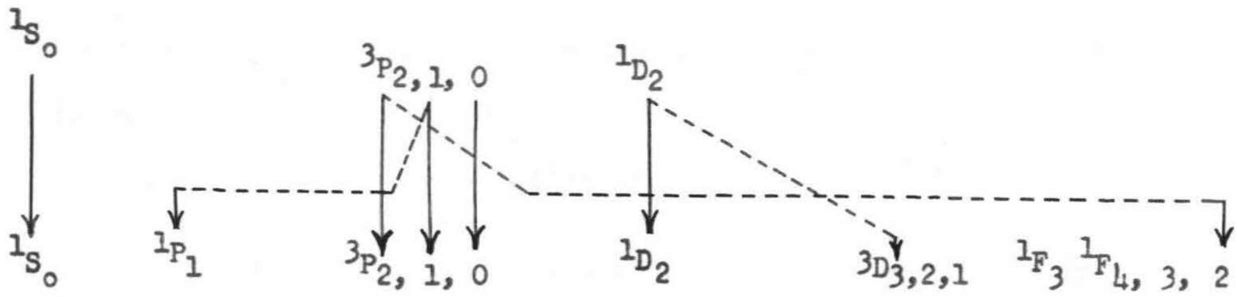

Without spin-orbit coupling, only the transitions indicated by the solid lines can occur. Spin-orbit coupling may produce, in addition, the transitions indicated by the dashed lines. In this case total angular momentum is still conserved, but spin and orbit quantum numbers may change in the transition. Conservation of parity requires that even and odd orbital states not mix.

For the present work spin-orbit coupling will be neglected. In the notation of references 30 and 31, the cross section may then be written,

$$d\sigma/d\Omega = \left| \sum_{\ell} \alpha_{\ell} g_{\ell}^{1/2} \sigma_{\ell}^{1/2} Y_{\ell 0} \right|^2 \qquad \text{(V-8)}$$

where $Y_{\ell o}$ is the normalized Legendre polynomial of order ℓ, g_{ℓ} is a weight factor, 1 for the singlet and 3 for the triplet states, $|\alpha_{\ell}|^2$ is the "intrinsic reaction probability" characteristic of the ℓ'th partial wave, and

$$\sigma_{\ell} = (4/9)\pi \bar{\lambda}^2 (2\ell + 1)P_{\ell} \qquad \text{(V-9)}$$

where $\bar{\lambda}$ is the wave-length in center of mass coordinates of the (reduced) incident particle, and P_{ℓ} is the penetrability of the ℓ'th partial wave to the radius of interaction. The factor, 1/9, comes from the 9 initial spin states corresponding to a quintet, triplet, and singlet. The "4" comes from symmetrization of the wave function to include the fact that the interacting particles are identical. For P_ℓ the Gamow penetration factor was used. In this case,

$$P_\ell = \exp(-2C_\ell), \text{ where}$$

$$C_\ell = g\left\{(x^{-1/2}/2)\left[(\pi/2) + \sin^{-1}(1 - 2x)(1 + 4xy)^{-1/2}\right] - (y + 1 - x)^{1/2} + y^{1/2}\,\ell n\left[1 + 2y^{1/2}(y^{1/2} + (y + 1 - x)^{1/2})\right]\left[1 + 4xy\right]^{-1/2}\right\} \quad \text{(V-10)}$$

and

$$y = \left[(\ell + 1/2)/g\right]^2$$

$$g = (0.0694\ ZZ'RM)^{1/2}$$

$$x = 0.694\ E_cR/ZZ'$$

where R is the radius of the interaction in units of 10^{-13} cm, E_c is the energy in center of mass coordinates, Z,Z' are the atomic numbers of the interacting nuclei, and M is the reduced mass in units of the proton mass.

α_o, α_1, α_2, and R are to be adjusted to fit the experimental results. Since the present results give the total cross section, it is convenient to integrate (V-8) over the sphere. This gives

$$\sigma_T/\sigma_o = |\alpha_o|^2 + 9|\alpha_1|^2\ P_1/P_o + 5|\alpha_2|^2\ P_2/P_o \quad \text{(V-11)}$$

(V-8) may be expanded to obtain

$$4\pi d\sigma/d\Omega = (1 + A\cos^2\theta + B\cos^4\theta)(1 + A/3 + B/5)^{-1} \quad \text{(V-12)}$$

and (V-11) may be written

$$\sigma_T/\sigma_o = D(1 + A/3 + B/5) \quad \text{(V-13)}$$

where now

$$DA = 27|\alpha_1|^2\ P_1/P_o + 15|\alpha_o||\alpha_2|\cos\chi(P_2/P_o)^{1/2} - 75|\alpha_2|^2\ P_2/2P_o \quad \text{(V-14)}$$

$$DB = 225|\alpha_2|^2 \; P_2/4P_o \qquad \text{(V-15)}$$

$$D = |\alpha_o|^2 - 5|\alpha_o| \; |\alpha_2| \cos\chi \, (P_2/P_o)^{1/2} + 25|\alpha_2|^2 \; P_2/4P_o \qquad \text{(V-16)}$$

Experimental values of σ_T, A, and B determine D through (V-13). $|\alpha_2|^2$ is then determined through (V-15) by the experimental value of B. (V-11) may be rewritten

$$\sigma_T/\sigma_o - 5|\alpha_2|^2 \; P_2/P_o = |\alpha_o|^2 + 9|\alpha_1|^2 \; P_1/P_o \qquad \text{(V-17)}$$

Plotting the left side of (V-17) against $9P_1/P_o$ should give a straight line with intercept, $|\alpha_o|^2$, and slope, $|\alpha_1|^2$. Having determined $|\alpha_o|^2$, $|\alpha_1|^2$, and $|\alpha_2|^2$, we may choose χ, the phase angle in the S-D interference term, to fit A. It should be noticed that necessarily $|\alpha_\ell|^2 \leq 1$, and in this case since there are two reactions of approximately equal probability, $|\alpha_\ell|^2 \leq 0.5$.

With R = 7, the value used in refs. 30 and 31, and with $\cos\chi = -1.0$, $|\alpha_o|^2 = 0.0175$, $|\alpha_1|^2 = 0.027$, and $|\alpha_2|^2 = 0.14$, a good fit to σ_T, A, and B (or the Legendre polynomial coefficients C_2 and C_4) is obtained for energies above 150 kev (Figs. 3 and 19). At low energies the fit in the angular coefficients is not bad and is within experimental uncertainties. But the 20% difference in total cross section obtained is outside experimental uncertainties. The total cross section fit is not affected much by the size of $|\alpha_2|^2$. The effect of the D-wave on the angular distribution comes largely from the S-D interference term for which the barrier factor $(P_oP_2)^{1/2}$ behaves approximately like P_1. Interference between terms of different parity is forbidden by the necessary symmetry of a reaction involving identical particles.

A fit of the low energy data ($E_1 \leq 150$ kev) can be obtained only with much less P-wave and somewhat more S-wave, but in this case the total cross section does not rise rapidly enough above 150 kev. This is the situation that led Beiduk, et al.(31) to introduce spin-orbit coupling. The use of a larger radius (R = 12) permits the total cross section above 150 kev to be fitted with the introduction of practically no S-wave interaction, but the data below 150 kev is not fitted any better.

One is tempted to say that the conclusion of Beiduk, et al. that spin-orbit forces are needed to explain the interaction are still valid. However, conclusions based on results achieved with so simplified a model of the interaction must be conservative. Given nuclear boundary conditions are not fitted accurately by the W.K.B. method in the energy region near the top of the barrier. A better representation could probably be obtained by the calculation of the reaction width from the Coulomb wave function tables of Breit, et al., following the procedure of Christy and Latter(62).

A more fundamental objection arises from the use of a fixed radius for the interaction. Since the deuteron has a large radius, it is to be expected that the interaction will involve a relatively large region of space. Although complications introduced by the Coulomb field would add considerably to the numerical problems, it is to be hoped that the problem can be attacked with the explicit introduction of information concerning the internal structure of the deuteron.

REFERENCES

1. Lawrence, Lewis, and Livingston, Letters, Phys. Rev. 44, 55 & 56, (1933).
2. Oliphant, Harteck, and Rutherford, Letter, Nature 133, 413 (1934).
3. Oliphant, Harteck, and Rutherford, Proc. Roy. Soc. A144, 692 (1934).
4. Cockcroft and Walton, Proc. Roy. Soc. A144, 704 (1934).
5. Manley, Coon, and Graves, Abstract, Phys. Rev. 70, 101 (1946)
6. Graves, A.C., Graves, E.R., and Manley, Abstract, Phys. Rev. 70, 101 (1946).
7. Dee, Letter, Nature, 133, 564 (1934).
8. Dee, Proc. Roy. Soc. A148, 623 (1935).
9. Alexopoulos, Helv. Phys. Acta, 8, 513 & 601 (1935).
10. Burhop, Proc. Camb. Phil. Soc. 32, 643 (1936).
11. Bonner and Brubaker, Phys. Rev. 49, 19 (1936).
12. Döpel, Ann. d. Phys. (Lpzg), 28, 87 (1937).
13. Wetterer, Ann. d. Phys. (Lpzg), 30, 284 (1937).
14. Amaldi, Hafstad, and Tuve, Phys. Rev. 51, 896 (1937).
15. Roberts, Phys. Rev. 51, 810 (1937).
16. Ladenburg and Kanner, Phys. Rev. 52, 911 (1937).
17. Zinn and Seely, Phys. Rev. 52, 919 (1937).
18. Reddeman, Zeit. f. Phys. 110, 373 (1938).
19. Baldinger, Huber, and Staub, Helv. Phys. Acta, 11, 245 (1938).
20. Van Allen, Ellett, and Bayley, Letter, Phys. Rev. 56, 383 (1939).
21. Bennett, Mandeville, and Richards, Phys. Rev. 69, 418 (1946).
22. Coon, Davies, Graves, A.C., Graves, E.R., and Manley, U.S. Atomic Energy Commission Declassified Document MDDC 207.
23. Bretscher, French, and Seidl, Phys. Rev. 73, 815 (1948).

24. Blair, Freier, Lampi, Sleator, and Williams, Phys. Rev. 74, 1599 (1948).

25. Hunter and Richards, Phys. Rev. 76, 1445 (1949).

26. McNeill and Keyser, Phys. Rev. 81, 602 (1951).

27. Sanders, Moffatt, and Roaf, Phys. Rev. 77, 754 (1950).

28. French, PhD Thesis, Cambridge (1948).

29. Li, Whaling, Fowler, and Lauritsen, Phys. Rev. 83, 512 (1951).

30. Konopinski and Teller, Phys. Rev. 73, 822 (1948).

31. Beiduk, Pruett, and Konopinski, Phys. Rev. 77, 622 (1950).

32. Fowler, Lauritsen, and Lauritsen, Rev. Sci. Inst. 18, No. 11, 818-820 (Nov. 1947).

33. Morrish, Phys. Rev. 76, 1651 (1949).

34. Hall, PhD Thesis, California Institute of Technology (1948).

35. Lorrain, Canad. J. Res. A., 25, 338 (Nov., 1947).

36. Finkelstein, Rev. Sci. Inst. 11, 94 (1940).

37. Thoneman, Moffatt, Roaf, and Sanders, Proc. Phys. Soc. Lond. 61, 483 (Nov. 1948).

38. Snyder, Rubin, Fowler, and Lauritsen, Rev. Sci. Inst. 21, 852 (1950).

39. Judd, Rev. Sci. Inst. 21, 213 (1950).

40. Li, PhD Thesis, California Institute of Technology, (June 1951).

41. Whaling and Li, Phys. Rev. 81, 150 (1951).

42. Crenshaw, Phys. Rev. 62, 54 (1942).

43. Hall, Phys. Rev. 79, 504 (1950).

44. French and Seidl, Phil. Mag. 42, 537 (1951).

45. Hirshfelder and Magee, Phys. Rev. 73, 207 (1948).

46. Walske, PhD Thesis, Cornell University (1951).

47. Appleyard, Proc. Camb. Phil. Soc. 47, 443 (1951).

48. Philipp, Zeit. f. Phys. 17, 23 (1923).

49. Buechner, Strait, Sperduto, and Malm, Phys. Rev. 76, 1543 (1949).

50. Bartels, Ann. d. Physik 13, 373 (1932).

51. Keene, Phil. Mag. 40, 369 (1949).

52. Kanner, Phys. Rev. 84, 1211 (1951).

53. Fermi and Teller, Phys. Rev. 72, 399 (1947).

54. Bethe, Rev. Mod. Phys. 22, 213 (1950).

55. Henderson, Proc. Roy. Soc. A109, 157 (1925).

56. Briggs, Proc. Roy. Soc. A114, 341 (1927).

57. Rutherford, Phil. Mag. 47, 277 (1924).

58. Foldy, Phys. Rev. 83, 397 (1951).

59. Laubenstein and Laubenstein, Phys. Rev. 84, 18 (1951).

60. Thomas (to be published).

61. Bloch, Hull, Broyles, Bouricius, Freeman, and Breit, Rev. Mod. Phys. 23, 147 (1951).

62. Christy and Latter, Rev. Mod. Phys. 20, 185 (1948).

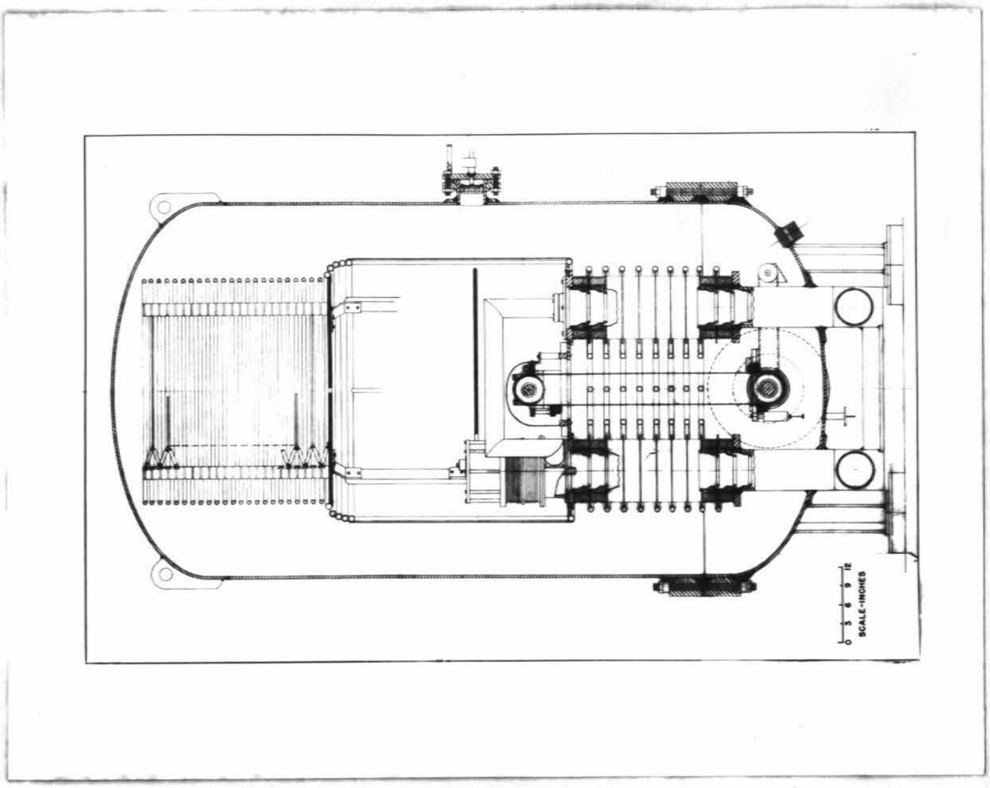

Fig. 1. ELECTROSTATIC GENERATOR

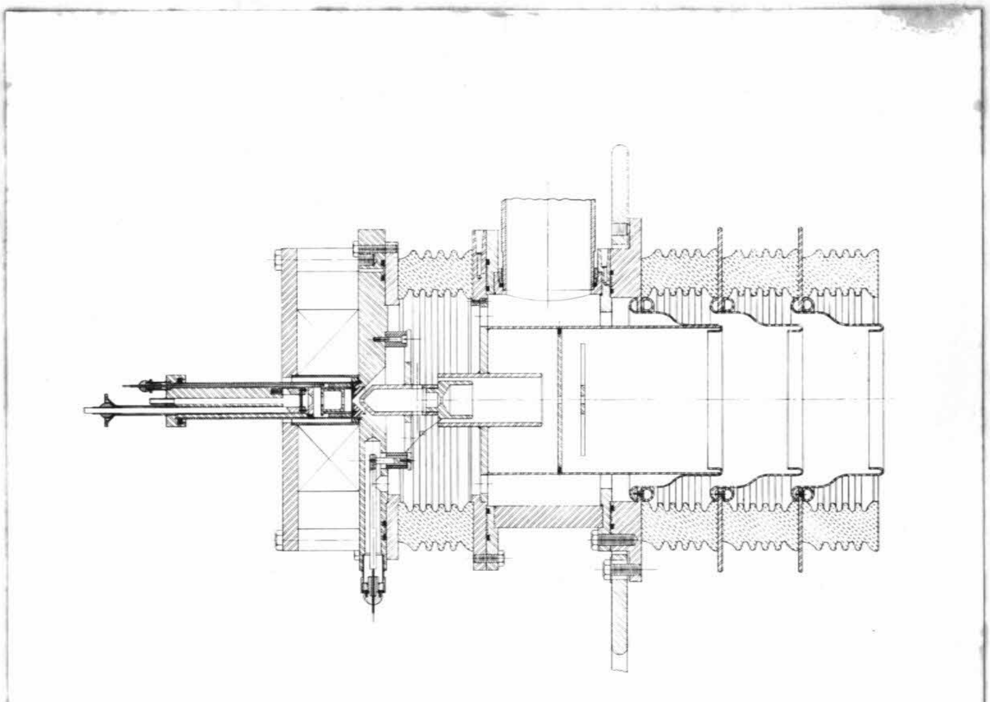

Fig. 2. ION SOURCE AND ION GUN

Fig. 3

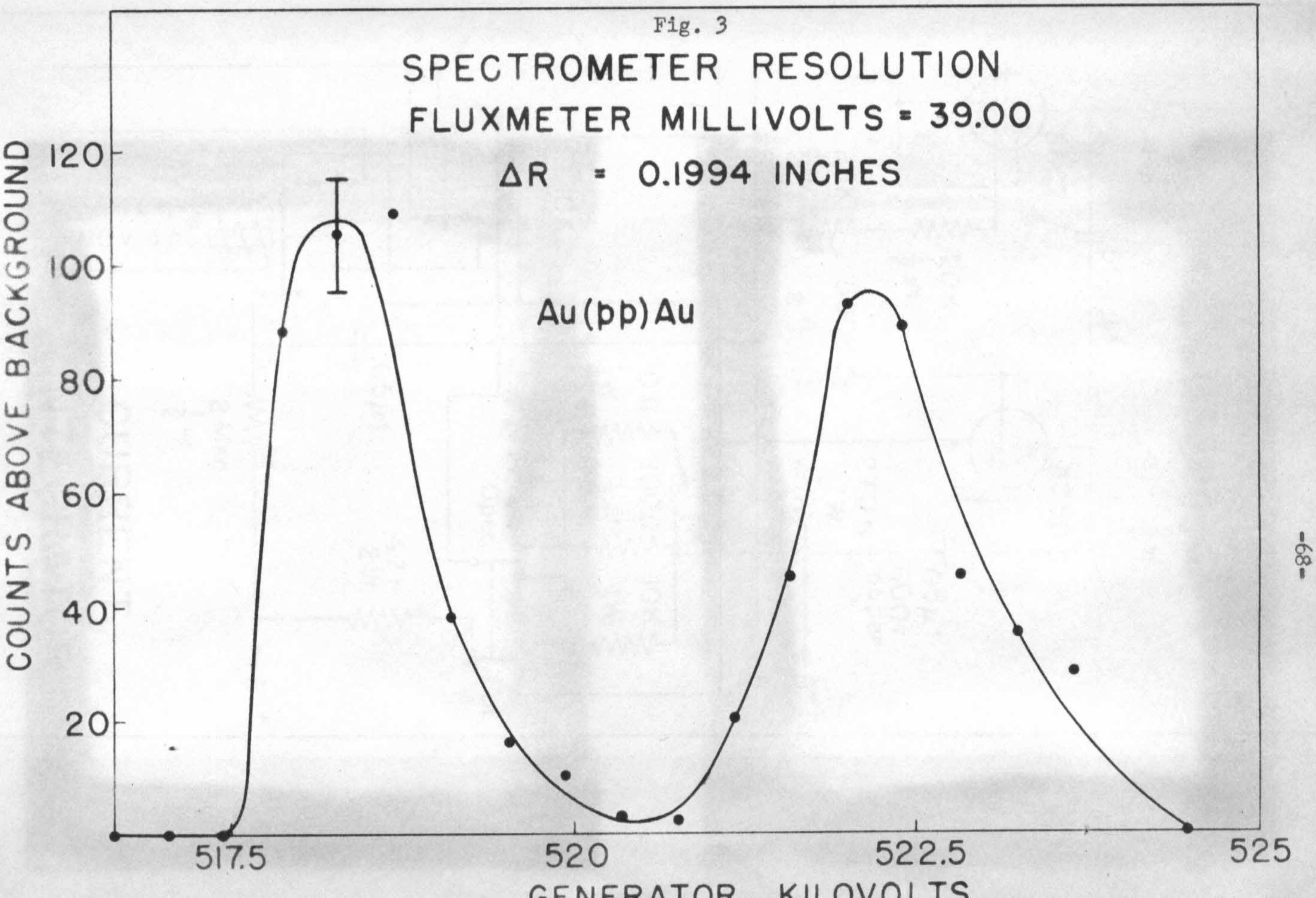

SPECTROMETER RESOLUTION

FLUXMETER MILLIVOLTS = 39.00

ΔR = 0.1994 INCHES

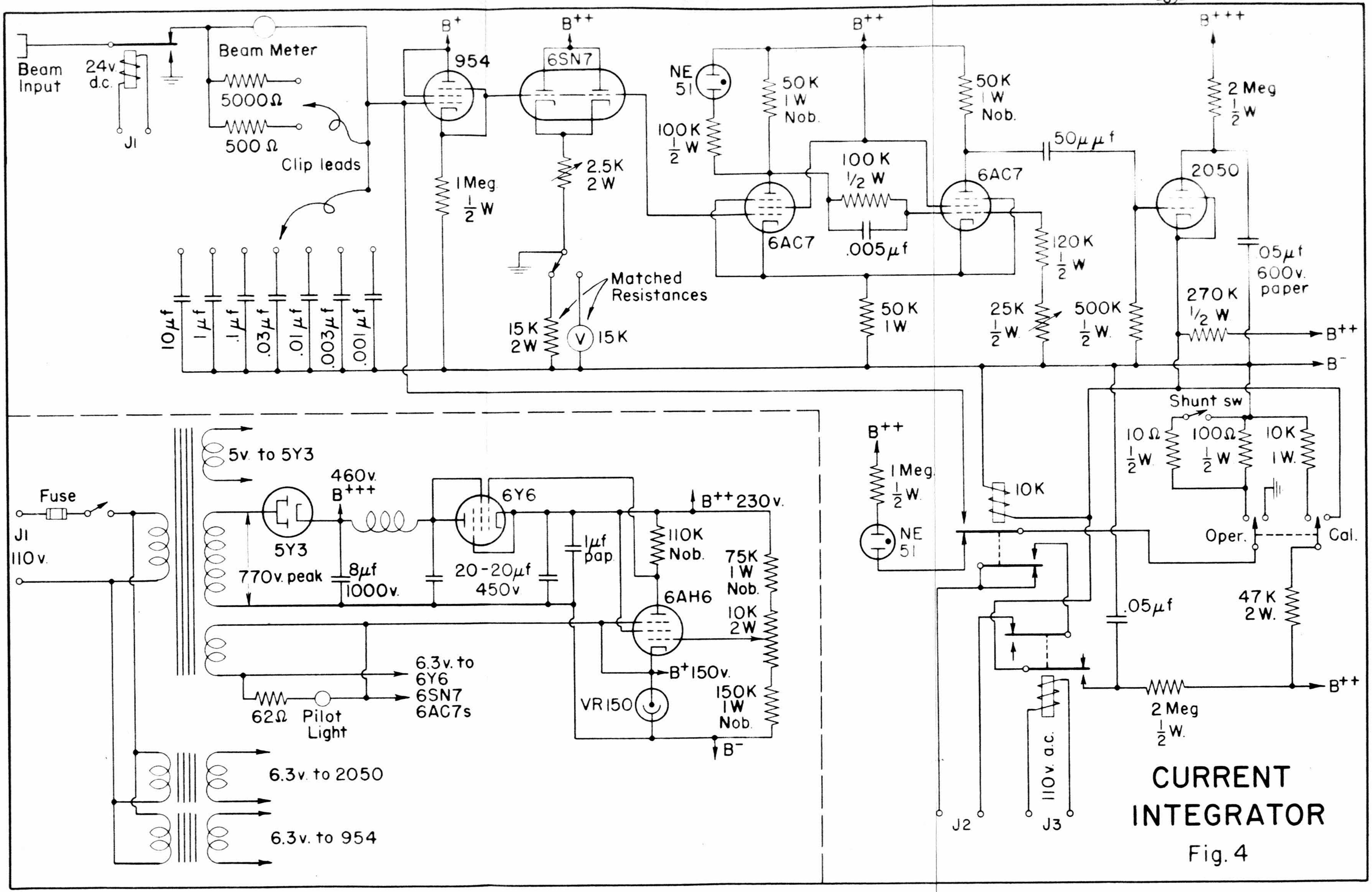

CURRENT INTEGRATOR

Fig. 4

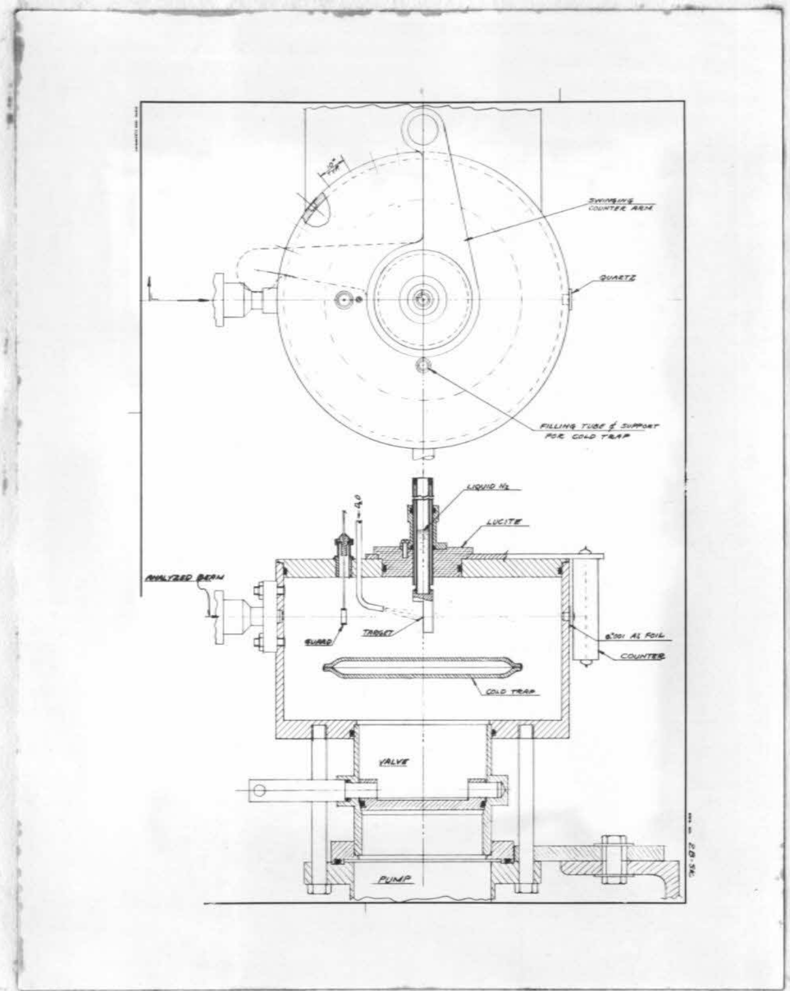

Fig. 5. ANGULAR DISTRIBUTION TARGET CHAMBER

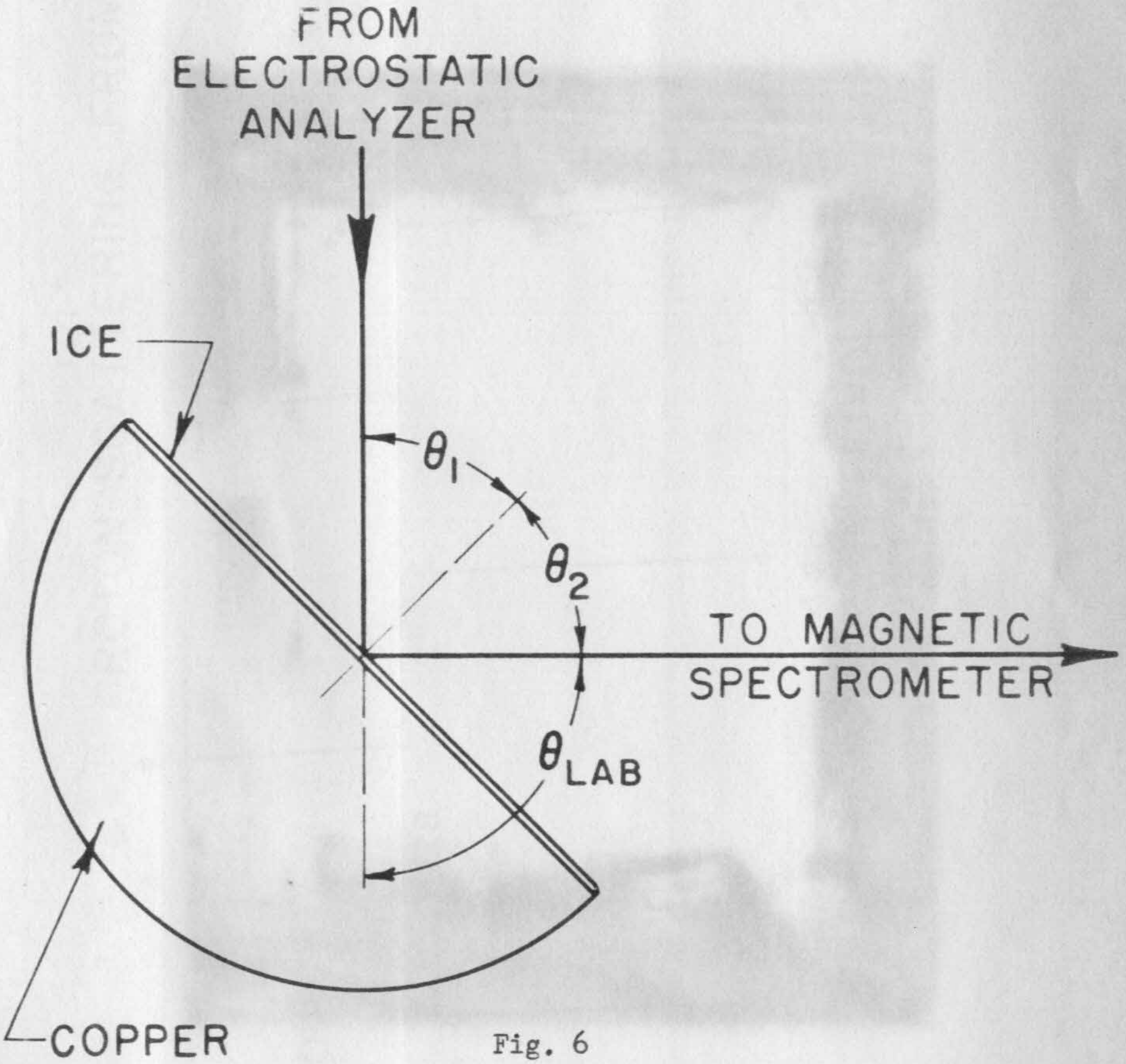
FROM
ELECTROSTATIC
ANALYZER
ICE
θ_1
θ_2
TO MAGNETIC
SPECTROMETER
θ_{LAB}
COPPER

Fig. 6

TARGET

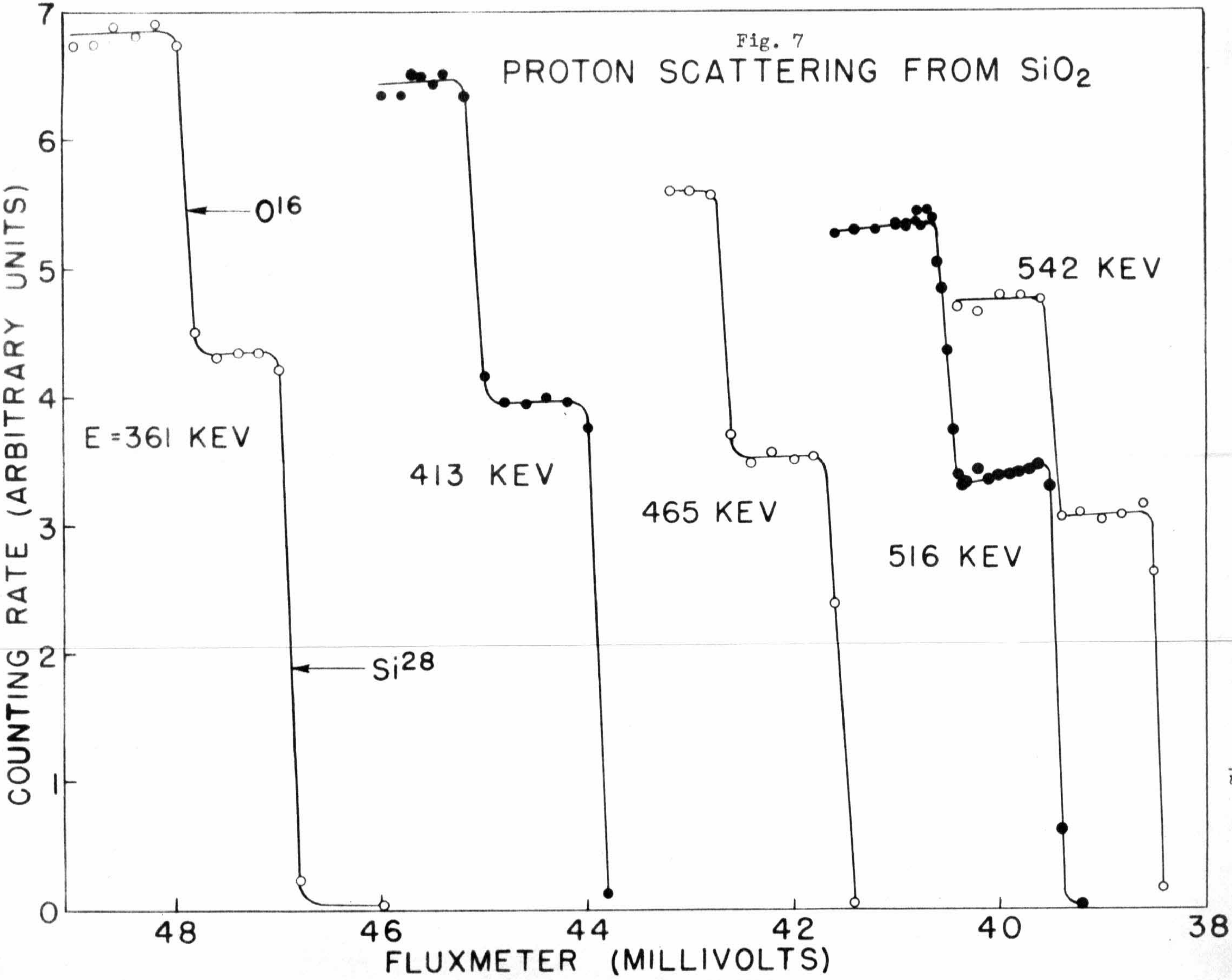

Fig. 7

PROTON SCATTERING FROM SiO_2

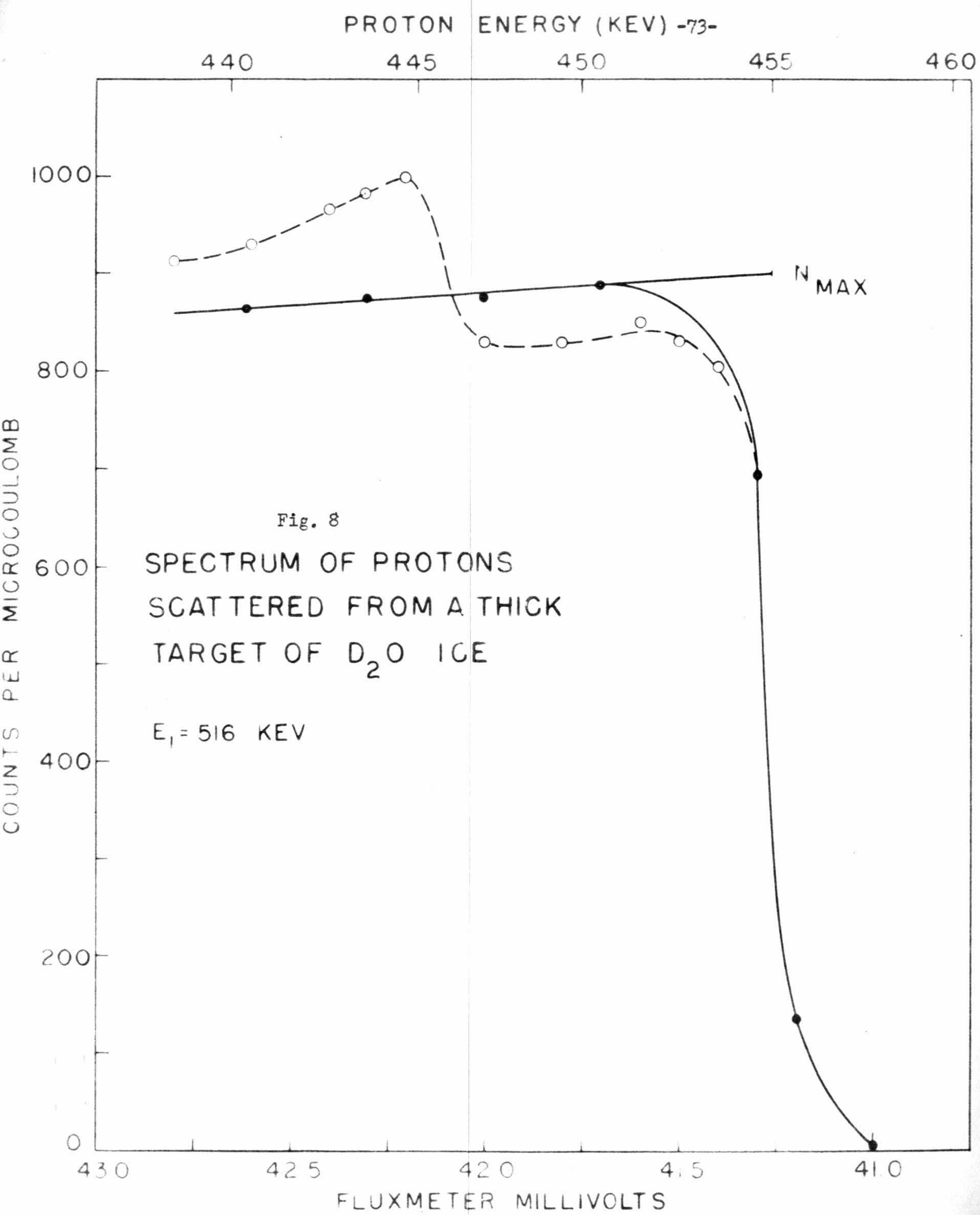

Fig. 8

SPECTRUM OF PROTONS SCATTERED FROM A THICK TARGET OF D_2O ICE

$E_1 = 516$ KEV

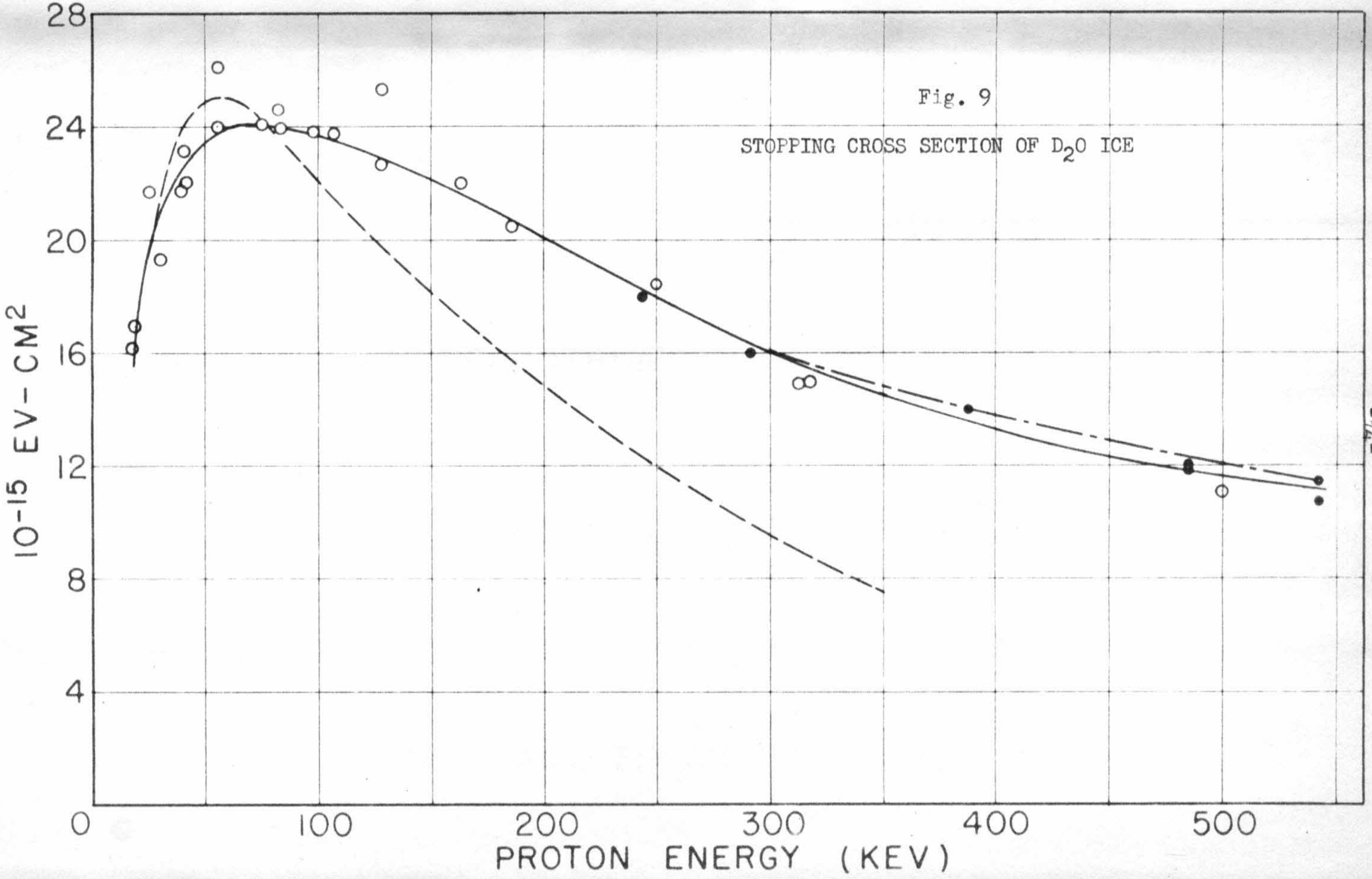

Fig. 9

STOPPING CROSS SECTION OF D_2O ICE

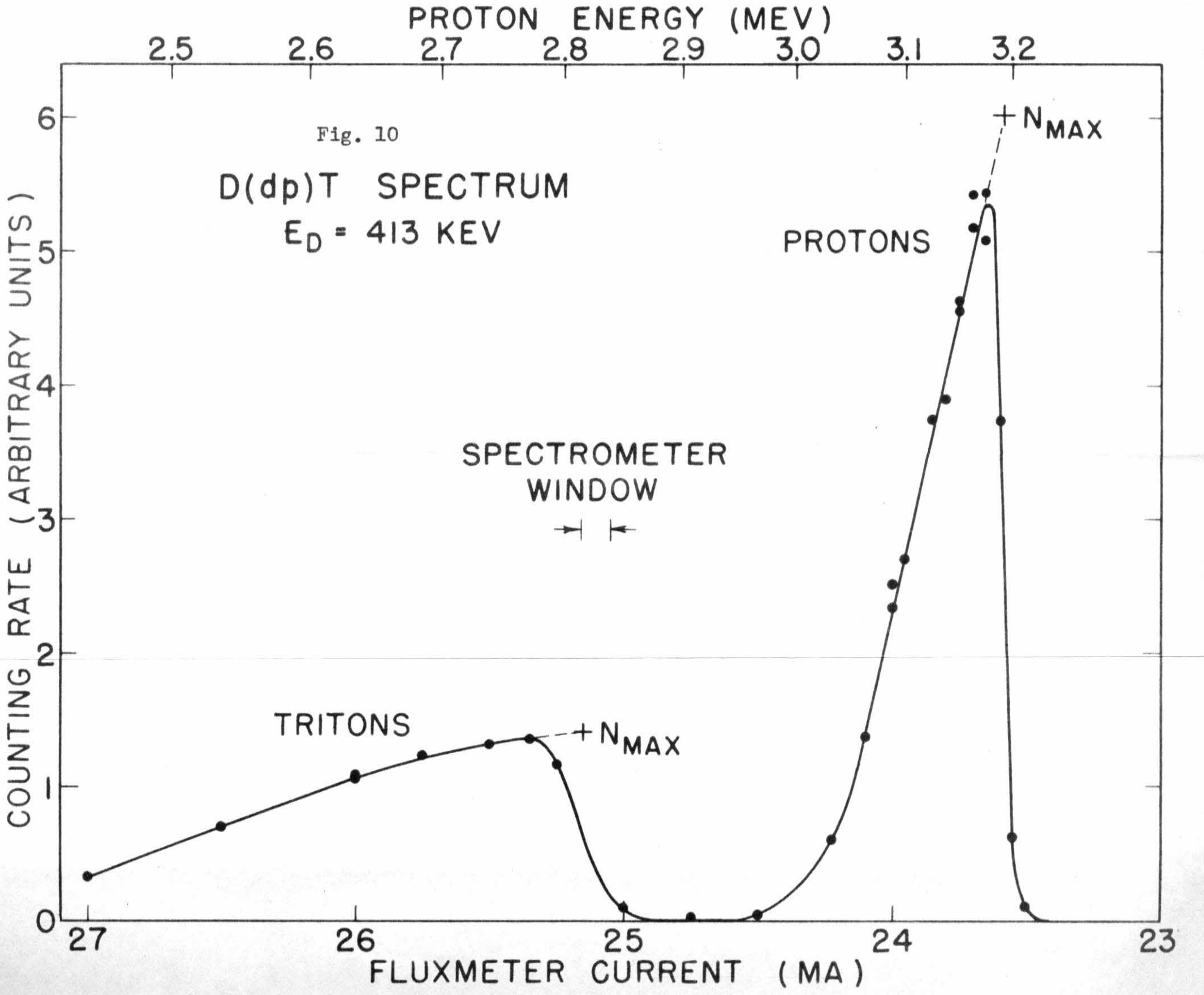

Fig. 10

D(dp)T SPECTRUM
E_D = 413 KEV
PROTON ENERGY (MEV)
2.5
2.6
2.7
2.8
2.9
3.0
3.1
3.2
COUNTING RATE (ARBITRARY UNITS)
0
1
2
3
4
5
6
+ N_{MAX}
PROTONS
SPECTROMETER WINDOW
TRITONS
+ N_{MAX}
27
26
25
24
23
FLUXMETER CURRENT (MA)

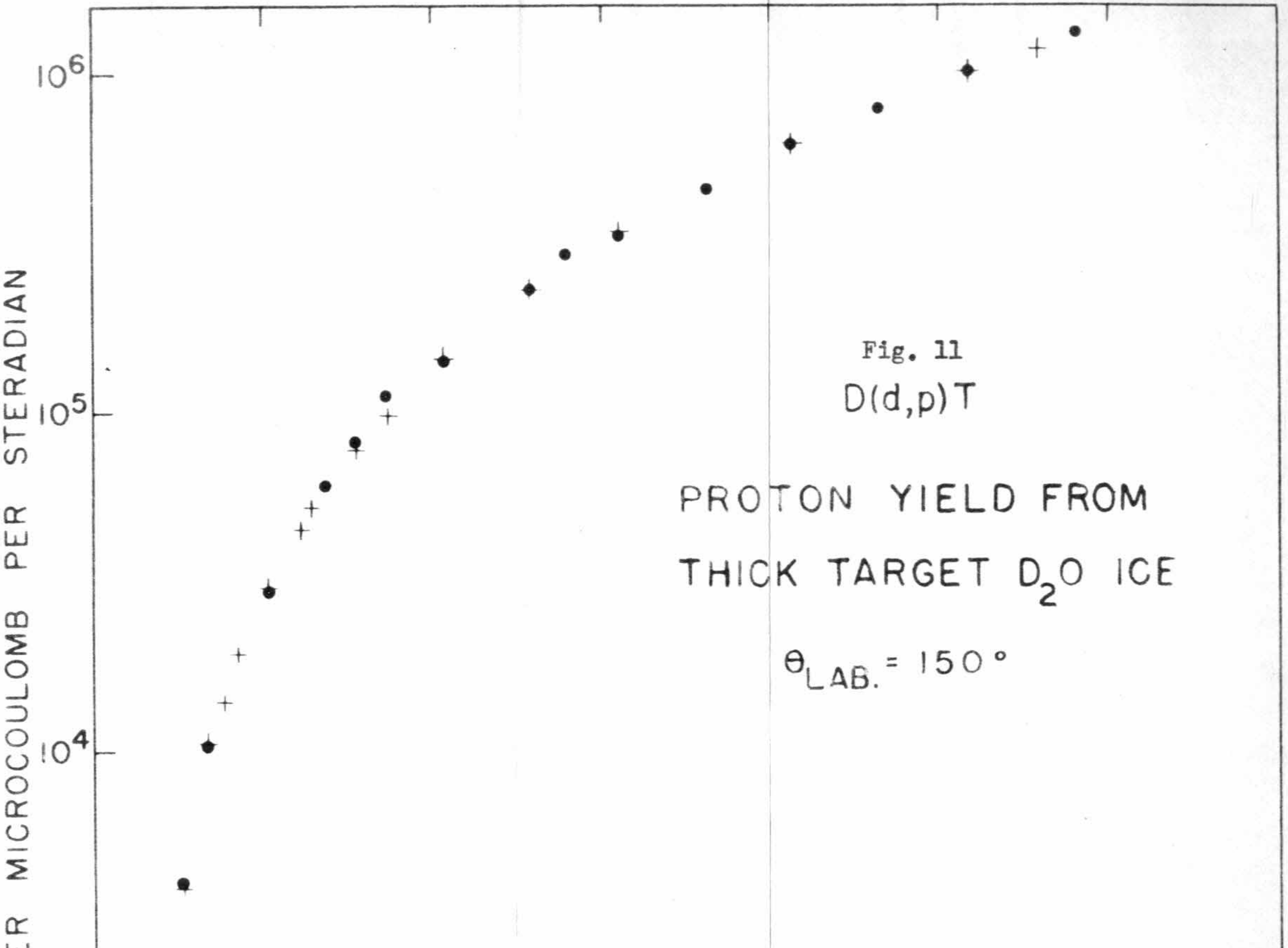

Fig. 11

D(d,p)T

PROTON YIELD FROM THICK TARGET D_2O ICE

$\theta_{LAB.} = 150°$

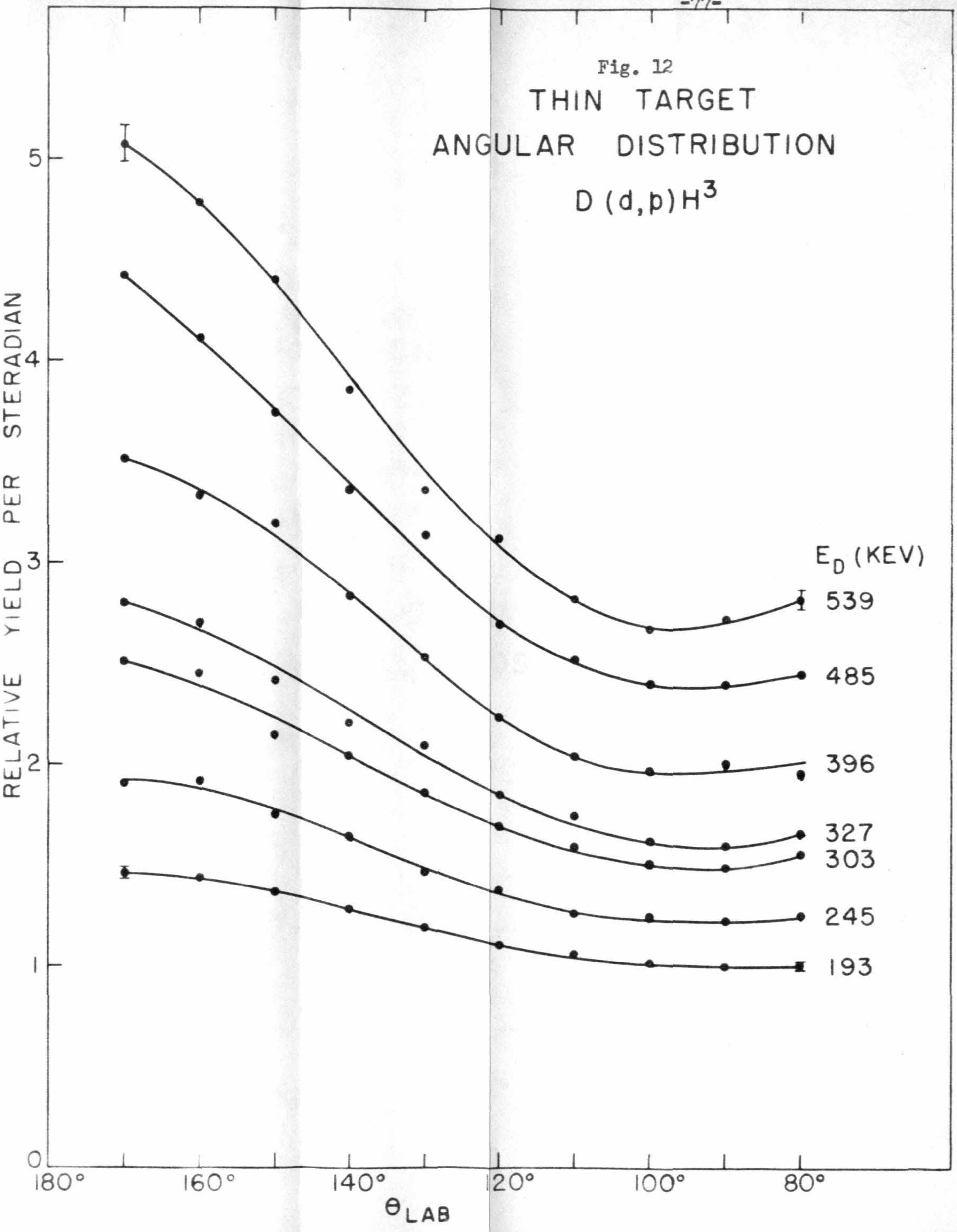
Fig. 12
THIN TARGET
ANGULAR DISTRIBUTION
D (d,p) H^3
RELATIVE YIELD PER STERADIAN
θ_{LAB}
E_D (KEV)
539
485
396
327
303
245
193
0
1
2
3
4
5
180°
160°
140°
120°
100°
80°

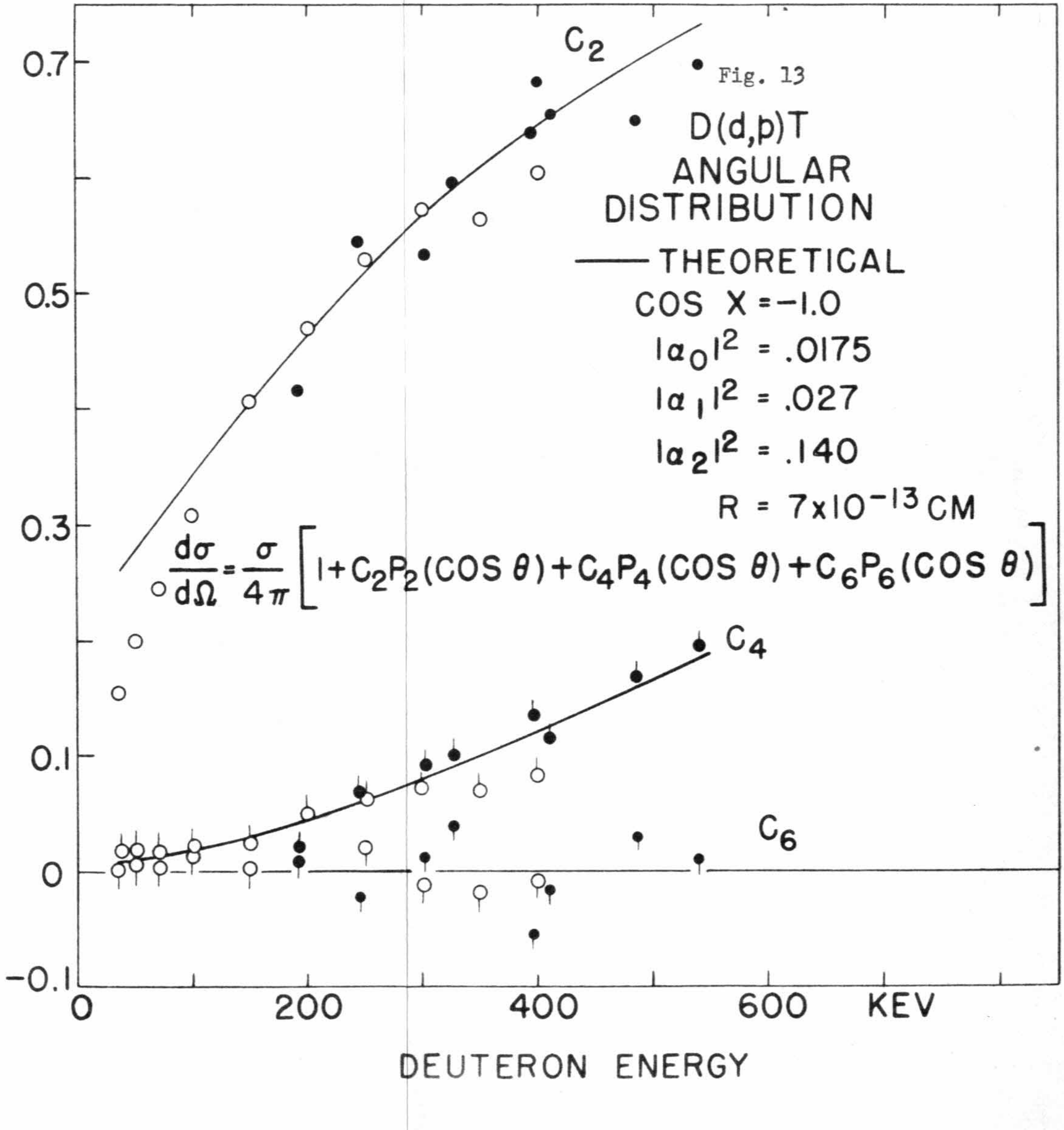

Fig. 13

C$_2$
C$_4$
C$_6$
● D(d,p)T
ANGULAR
DISTRIBUTION
—— THEORETICAL
COS X = −1.0
$|\alpha_0|^2$ = .0175
$|\alpha_1|^2$ = .027
$|\alpha_2|^2$ = .140
R = 7x10^{-13} CM
$\frac{d\sigma}{d\Omega} = \frac{\sigma}{4\pi}\left[1 + C_2P_2(\cos\theta) + C_4P_4(\cos\theta) + C_6P_6(\cos\theta)\right]$
0.7
0.5
0.3
0.1
0
-0.1
0
200
400
600
KEV
DEUTERON ENERGY

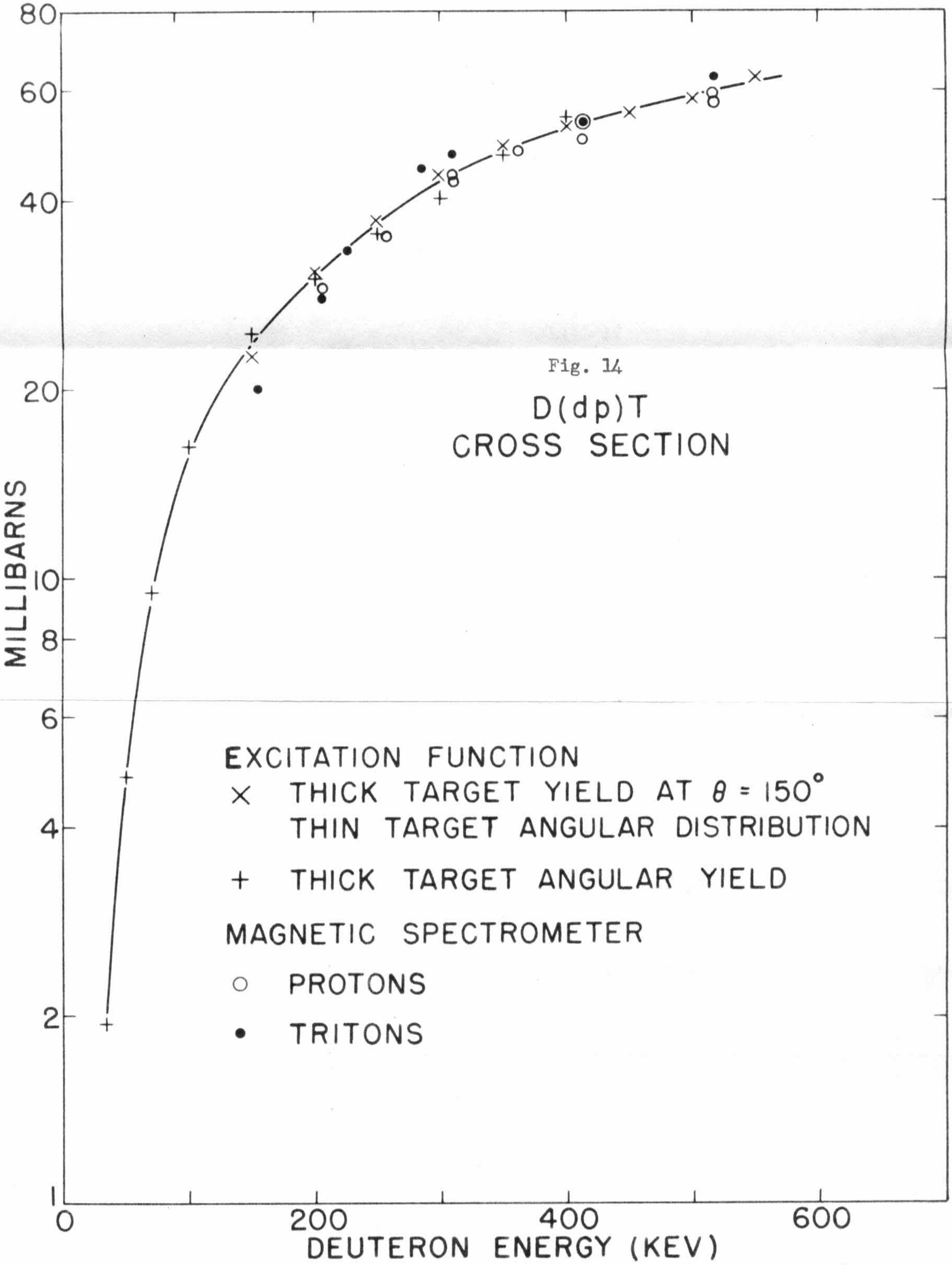

Fig. 14

D(dp)T
CROSS SECTION

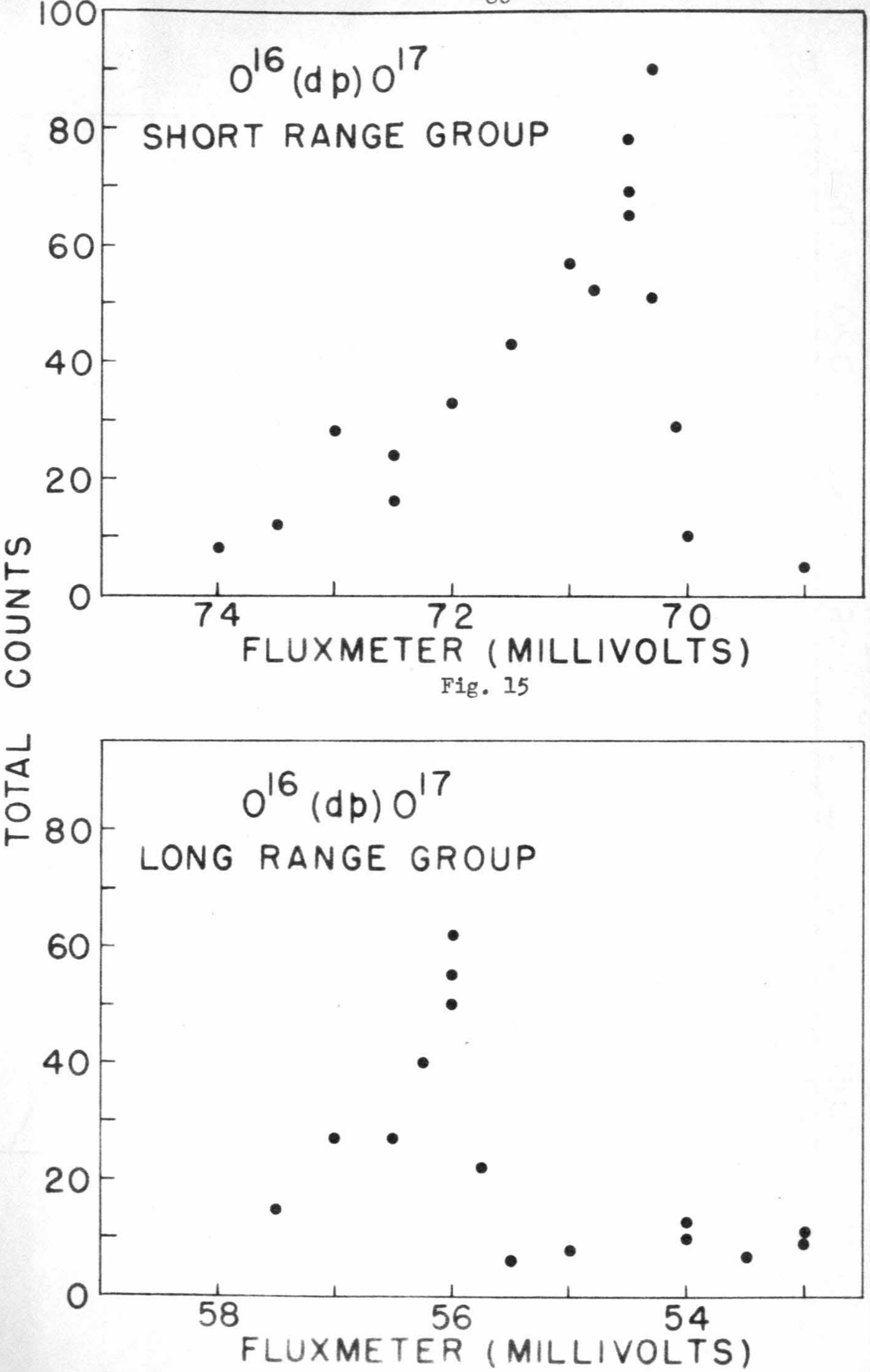
$O^{16}(dp)O^{17}$
SHORT RANGE GROUP
100
80
60
40
20
0
74
72
70
FLUXMETER (MILLIVOLTS)
TOTAL COUNTS
$O^{16}(dp)O^{17}$
LONG RANGE GROUP
80
60
40
20
0
58
56
54
FLUXMETER (MILLIVOLTS)

Fig. 15

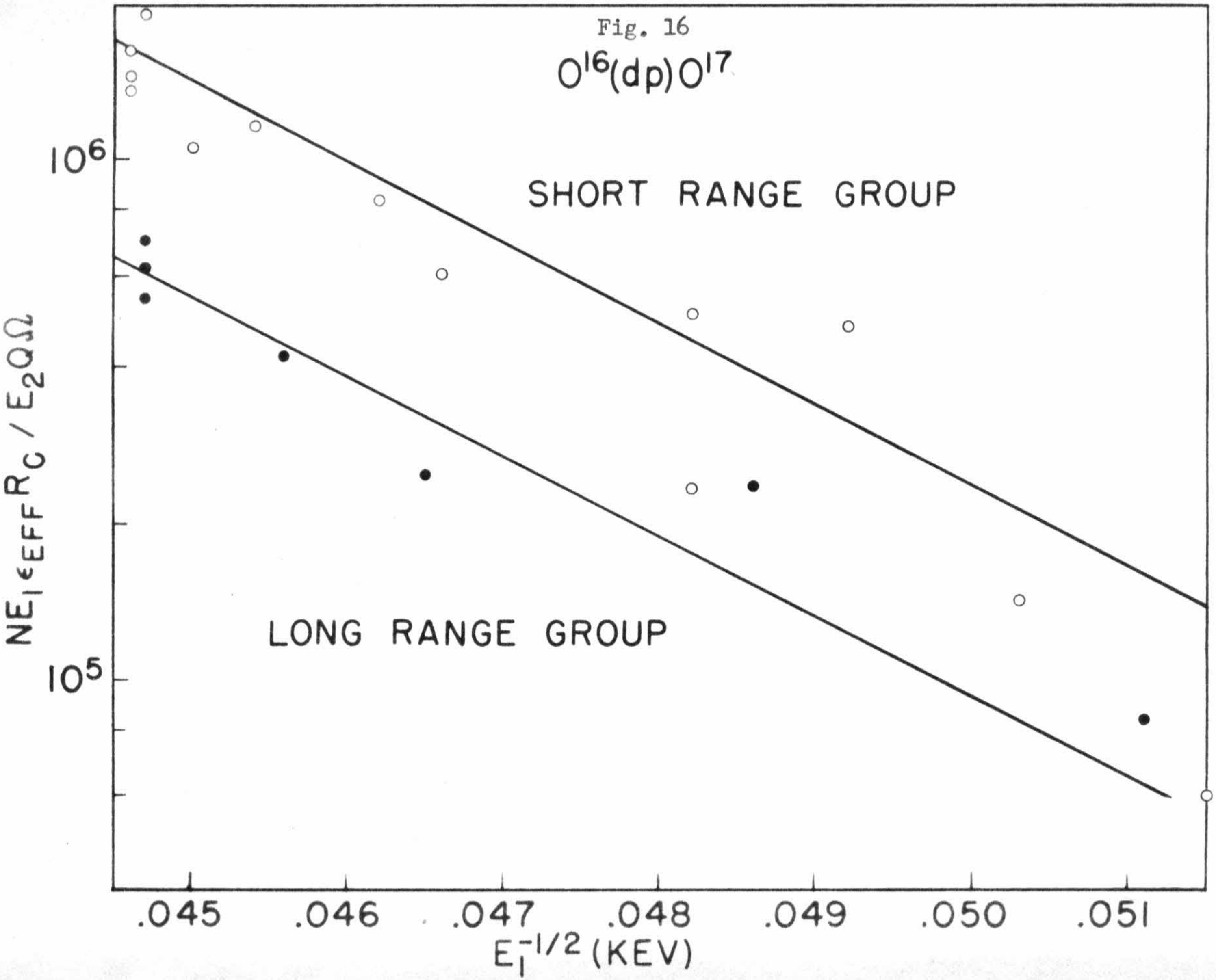

Fig. 16

$O^{16}(dp)O^{17}$
SHORT RANGE GROUP
LONG RANGE GROUP
$NE_1\epsilon_{EFF}R_C / E_2Q\Omega$
10^6
10^5
.045
.046
.047
.048
.049
.050
.051
$E_1^{-1/2}$ (KEV)

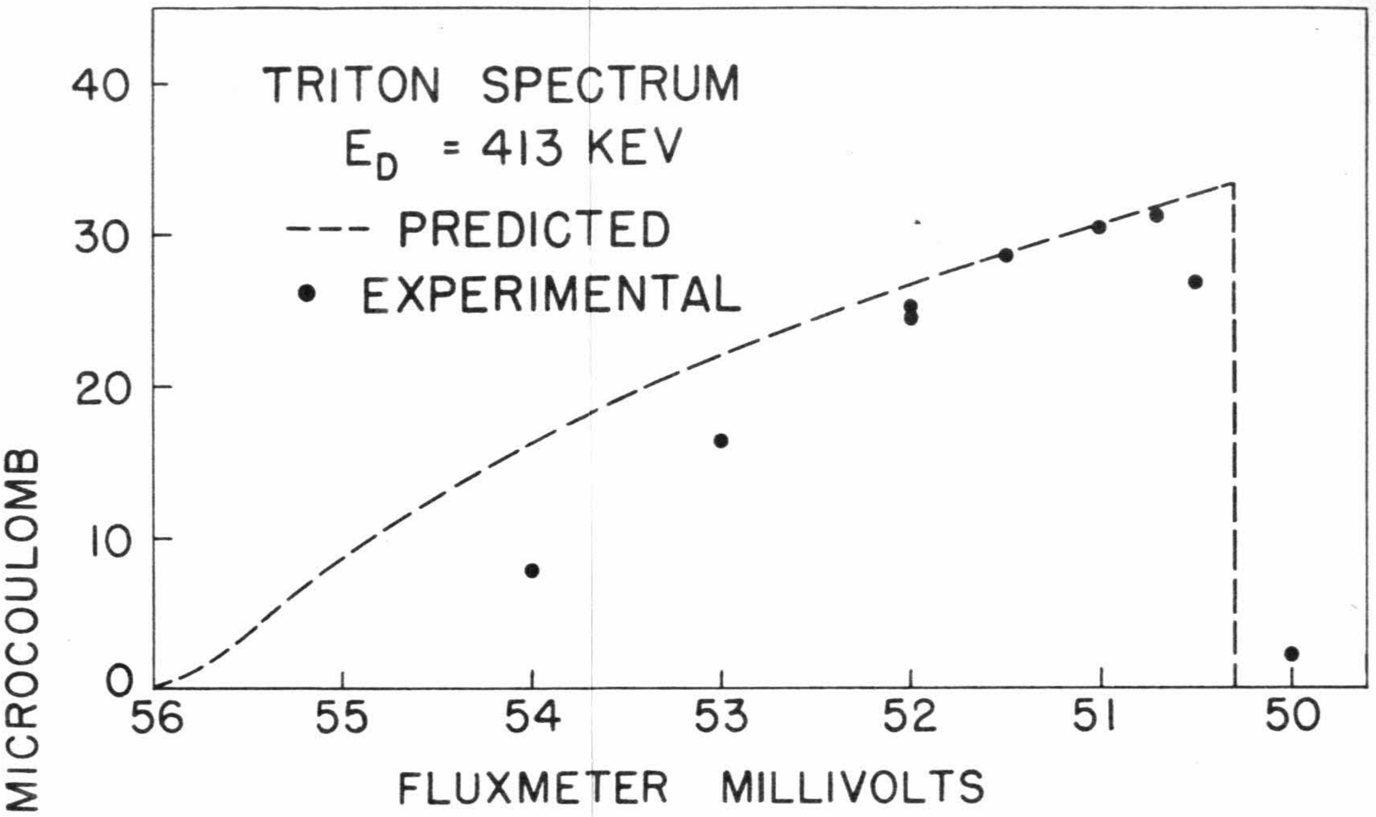
TRITON SPECTRUM
E_D = 413 KEV
--- PREDICTED
● EXPERIMENTAL
COUNTS PER MICROCOULOMB
40
30
20
10
0
56
55
54
53
52
51
50
FLUXMETER MILLIVOLTS

Fig. 17

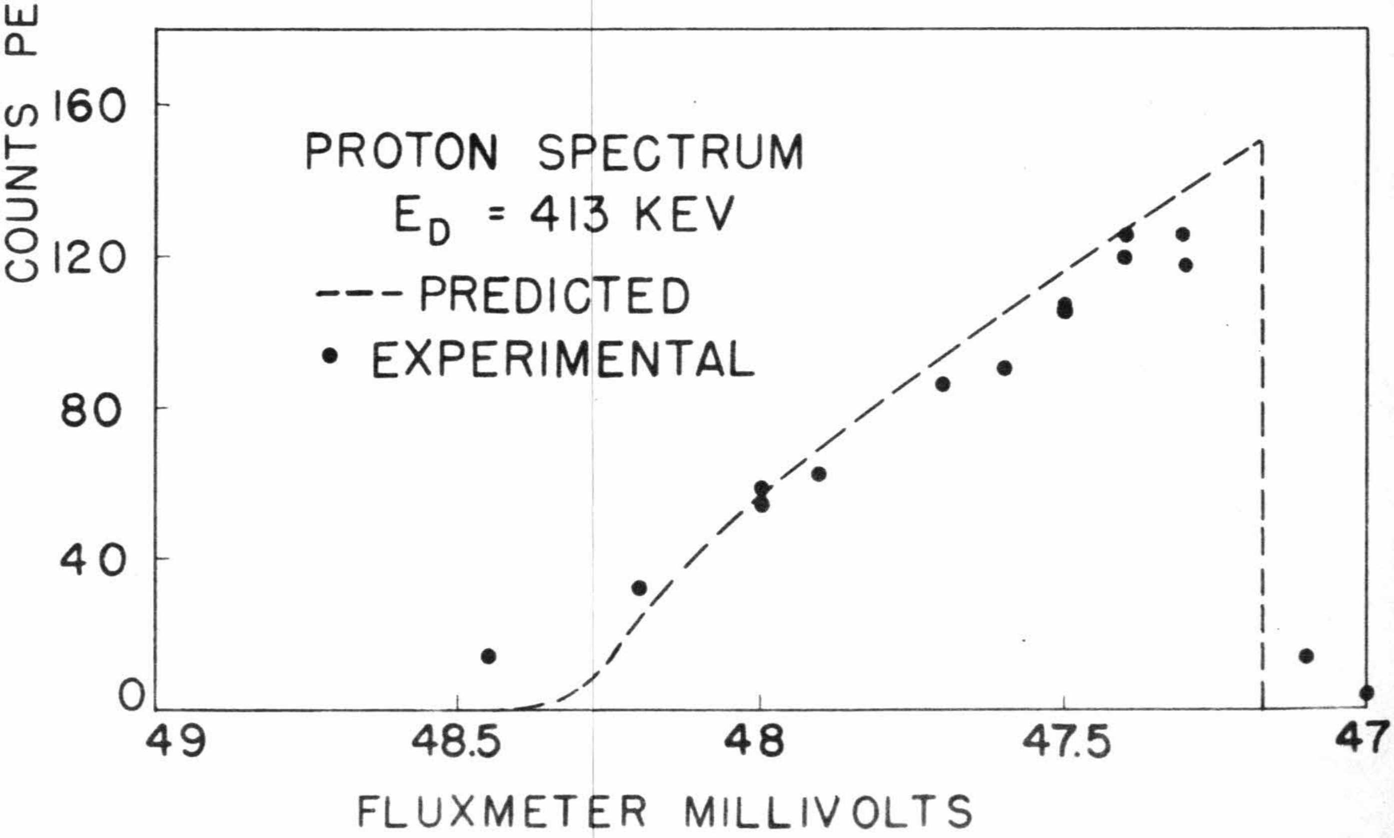
PROTON SPECTRUM
E_D = 413 KEV
--- PREDICTED
● EXPERIMENTAL
160
120
80
40
0
49
48.5
48
47.5
47
FLUXMETER MILLIVOLTS

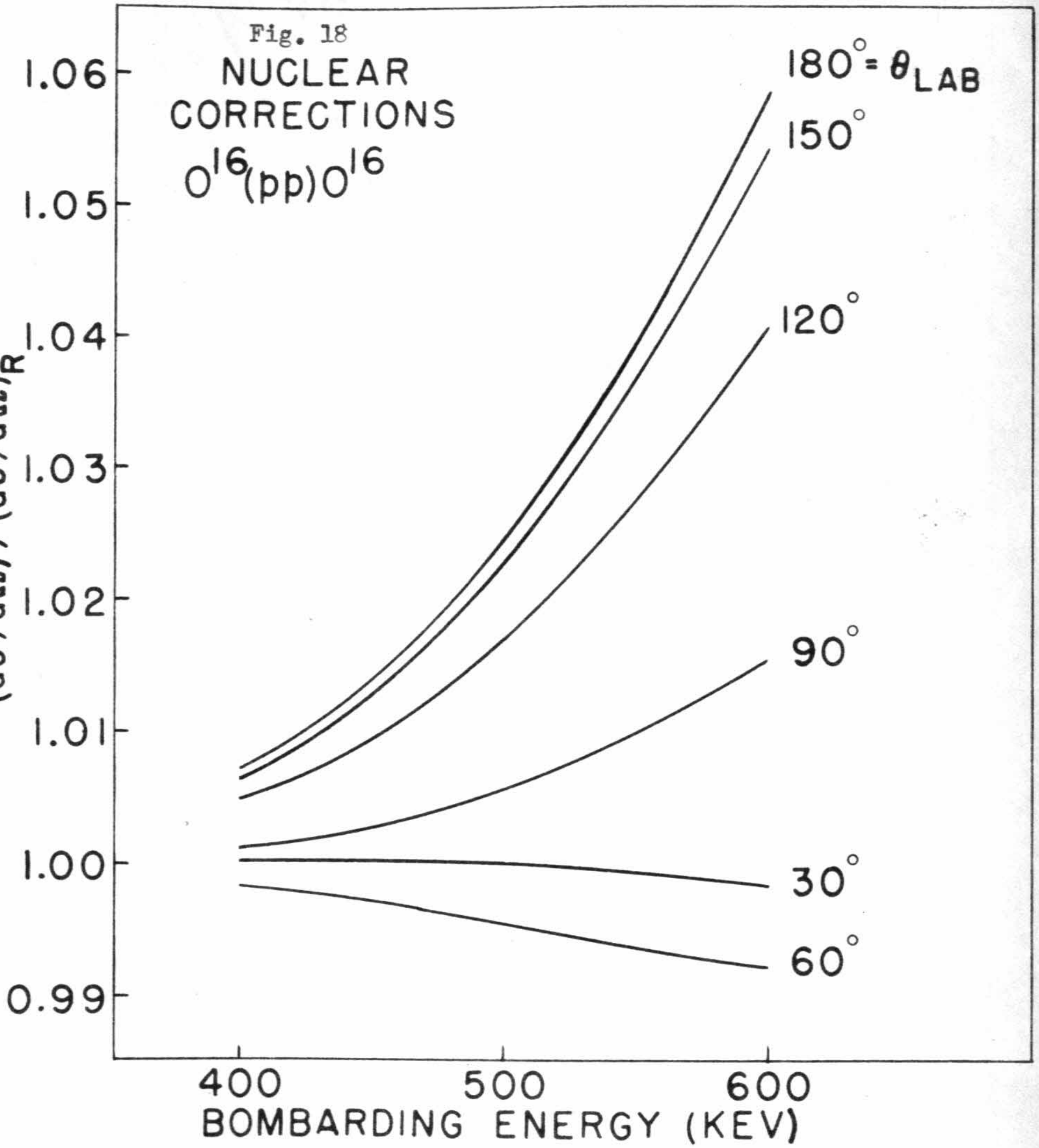
Fig. 18
NUCLEAR
CORRECTIONS
$O^{16}(pp)O^{16}$
$180^\circ = \theta_{LAB}$
150°
120°
90°
30°
60°
1.06
1.05
1.04
1.03
1.02
1.01
1.00
0.99
$(d\sigma/d\Omega)/(d\sigma/d\Omega)_R$
400
500
600
BOMBARDING ENERGY (KEV)

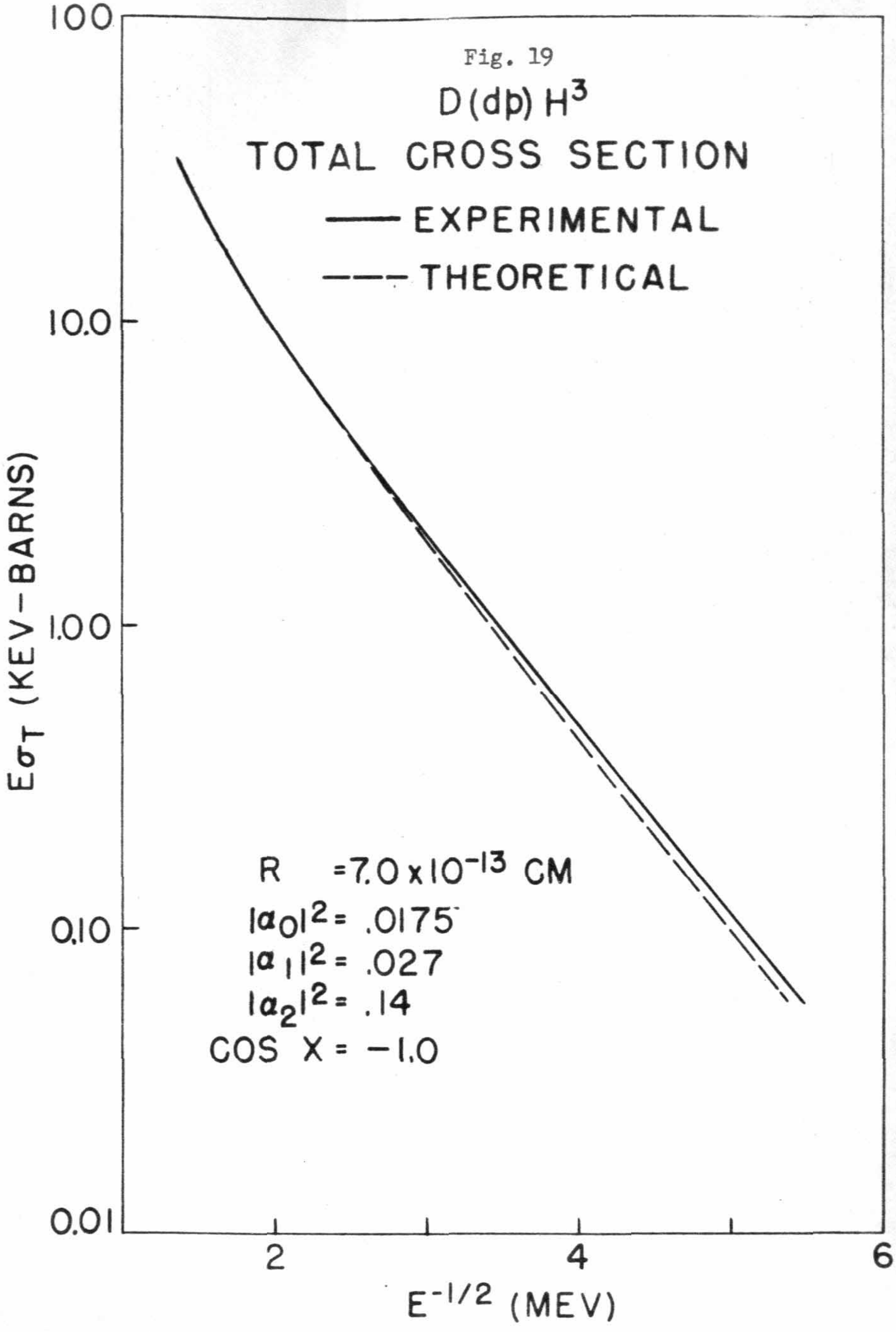

Fig. 19

$D(dp)H^3$

TOTAL CROSS SECTION